PHYSICAL REVIEW A **107**, 063514 (2023)

Scattered and guided radiation emitted by an electron moving near a dielectric rod

Matan Haller and Levi Schächter*
Technion–Israel Institute of Technology, Haifa 32000, Israel

(Received 14 October 2022; accepted 26 May 2023; published 27 June 2023)

The scattered and guided radiation excited by a point charge moving in the vicinity of an infinite, dielectric cylinder is considered. It is shown that guided waves constitute the dominant contribution to the emitted radiation for short distances between the particle and the cylinder, low yet relativistic particle energies (roughly $10^{-1} < \gamma - 1 < 10^{1}$, where γ is the Lorentz factor), and large cylinder permittivity. In all the complementary cases, radiation by scattered waves dominates the spectrum. Analytic, approximate expressions for the spectrum of the scattered radiation are presented, with the spectrum for high energies resembling that of plane-wave scattering. The relative contribution of the various cylinder eigenmodes to the guided radiation is also investigated. The effect of a finite-size bunch on the emitted radiation is considered. Finally, the number of emitted photons via both scattered and guided radiation is examined, with the scattered photon number observed to scale for high energies as $\ln(b\gamma)$.

DOI: 10.1103/PhysRevA.107.063514

I. INTRODUCTION

A charged particle moving in vacuum generates a spectrum of *evanescent* waves, each one propagating parallel to the particle's direction of motion and decaying exponentially in the perpendicular direction. What is unique about these waves is the fact that while the energy density is nonzero in both directions, the ability to do work (power) is viable in the longitudinal direction and identically zero perpendicular to the motion. The essence of any radiation source is to couple electromagnetic energy from an evanescent to a propagating wave. In the present paper, we examine a simple configuration consisting of a dielectric rod and a charge moving perpendicular to the axis, and we aim to establish the scaling laws which control the emitted spectrum in various regimes.

Throughout the years several coupling mechanisms have been identified and thoroughly investigated. Transition radiation, for example, occurs when the particle crosses the interface between two media [1], diffraction radiation occurs when the particle does not come in direct contact with an obstacle but only approaches it [2], bremsstrahlung ("braking radiation") occurs when the particle is dramatically decelerated [3], Čerenkov radiation occurs when the particle moves faster than the phase velocity of light in the surrounding medium [4], and Smith-Purcell radiation occurs when the particle traverses a periodic structure [5]. Radiation emitted due to interaction between evanescent fields induced by charged particles and dielectric or metallic structures is of high interest in various scientific and industrial applications, such as the design of optical accelerators [6], electron microscopy [7], and novel terahertz radiation sources [8], and in the last decade also for the realization of single-photon sources for quantum information purposes [9].

Virtually any scheme that can generate radiation, and thus decelerate electrons, may be used for acceleration. In the context of the present paper we may conceive inverse Smith-Purcell or inverse Čerenkov processes recently reviewed in Ref. [6]. Such accelerating systems are driven by high-power lasers that are injected into dielectric structures (preferred over their metallic counterparts due to larger laser damage threshold and lower ohmic losses), and offer a promising alternative to conventional radio-frequency accelerators due to reduction in size (from meters to millimeters), required energy for acceleration, and operating costs. The emitted wakefield leads to both a decelerating force on the particle and a transverse "kick," which deflects the particle from its original trajectory, leading to a reduction in acceleration efficiency. Thus, a great effort is invested in minimizing the wakefields induced by the acceleration structures [6]. Besides acceleration considerations, the emitted wakefields may assist in beam diagnostics, that is, characterization of a charged bunch's spatial distribution, energy, and position relative to the structure [10–12].

An additional direct application of the interaction between structures and charge-induced evanescent fields is in electron microscopy. The resolution of conventional optical microscopes is limited by the wavelength of light (hundreds of nanometers), preventing the imaging of objects in the nanoscale (smaller than the wavelength of light). Electron microscopy solves this problem by using an electron as a source of illumination, which has a de Broglie wavelength several orders of magnitude smaller than light (roughly 1.7 pm for a 70-keV electron) [7]. The measurement of the electron's energy loss after traversing near the sample is known as *electron energy-loss spectroscopy* [13], and has been extensively used to characterize its interaction with micrometer- and nanometer-scale structures [14]. Another prevalent technique is *electron holography*, in which the electron passing through the sample is interfered with a reference electron

---

[*] levis@technion.ac.il

beam (passing through vacuum), with the interference performed via a very thin wire with positive voltage [15].

A particular structure of high interest, which is also the focus of this paper, is an infinite dielectric rod, which serves as an idealized optical fiber. More generally, it can model any corner or wedge in a dielectric structure with a similar radius of curvature. The coupling between a point charge's evanescent waves and the cylindrical structure induces electromagnetic radiation, with the radiated energy having two components: The first contribution comes from the scattering of radially propagating waves, which is a manifestation of diffraction radiation [2]. The second contribution comes from the excitation of guided modes inside the cylinder, which carry energy along its axis. The following can be roughly conceived as Ĉerenkov radiation emitted by image charges inside the dielectric medium.

Studies of electrodynamics in cylindrical structures date back to the beginning of the 20th century, with the works of Sommerfeld, who investigated wave propagation in resistive wires [16], and Hondros and Debye, who considered a lossless dielectric cylinder [17]. Since then, full analytical electromagnetic descriptions for the scattering of propagating (not evanescent) plane waves from a dielectric cylinder [18] and for its guided mode characteristics [19] have been formulated, rendering both close problems from a theoretical perspective.

Radiation due to coupling between cylindrical geometries and evanescent fields has also been studied for a point charge moving parallel to the cylinder's axis [20,21], a uniform line charge moving perpendicular to the cylinder's axis [22], and a planar beam with sinusoidal charge modulation moving in the same manner [23]. It should be noted that in the first two works no scattering is present due to the absence of an obstacle in the electron's direction of motion, and in the latter two studies no guided modes are excited due to translation symmetry along the cylinder's axis. The more complex case of a point charge moving perpendicular to the cylinder's axis has been investigated for metallic cylinders (with Drude permittivity) and arrays of cylinders in the context of surface plasmons [24,25]. However, these two studies lack analysis of the radiation carried by the guided modes, which are expected to emerge in such a configuration. The inverse effect to "wakefield recoil," namely, the acceleration of charged particles by field injection into dielectric structures, has also been theoretically [26], numerically [27], and experimentally [28] studied for a periodic cylindrical grating, which is a possible topology for a dielectric laser accelerator [6].

The remainder of this paper is organized as follows: In Sec. II we present a theoretical formulation for the electromagnetic fields formed inside the system and provide integral expressions for both the radially emitted (scattered) and axially emitted (guided) energy. In Sec. III we numerically evaluate the emitted energy and its spectrum, compare between the contributions of the scattered and guided waves, and examine their dependence on the various parameters of the system. Finally, in Sec. IV we provide concluding remarks.

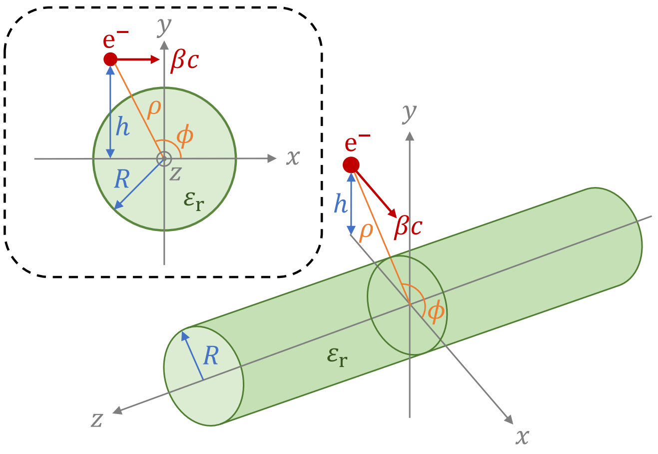

FIG. 1. The geometry of the system. An electron is moving in vacuum at a constant velocity βc in the x direction and with an impact parameter h above an infinite, dielectric cylinder of radius R and relative permittivity ε_r. The cylinder's axis coincides with the z axis. The electron's radial (ρ) and azimuthal (ϕ) coordinates are also depicted. The inset contains a two-dimensional projection of the geometry onto the xy plane.

II. ANALYTIC FORMULATION

A. Electromagnetic field

The system in consideration consists of a point charge, $-e$ representing a single electron, which moves in vacuum at a constant velocity $v = \beta c$ (c being the speed of light in vacuum), perpendicular to an infinite dielectric rod of radius R and relative permittivity ε_r (see Fig. 1). The electron's impact parameter relative to the cylinder's axis is $h > R$ and it moves in the x direction. We assume without loss of generality that at time $t = 0$ the electron is exactly above the cylinder, that is, $x = 0$. Moreover, it is assumed that the electron's longitudinal coordinate is $z = 0$. The coupling between the electron's evanescent fields and the cylindrical structure leads to the emission of radiation, causing the electron to experience a decelerating force, and as a result, in principle, it slows down. In practice, the emitted energy is several orders of magnitude smaller than the kinetic energy of the moving electron. Therefore, throughout this paper we assume that the electron's velocity is constant.

By virtue of the linearity of Maxwell's equations, we may represent the total field as a superposition of the electron's field in the absence of the cylinder, which we denote as the *primary* field, and the *secondary* field induced by the cylinder itself. We begin by evaluating the primary fields (superscript p): The longitudinal components (z) are given in space and time coordinates by (see Ref. [3] pp. 558–561)

$$\tilde{E}_z^{(p)}(\mathbf{r},t) = -\frac{e}{4\pi\varepsilon_0}\frac{\gamma z}{d^3(\mathbf{r},t)},$$
$$\tilde{H}_z^{(p)}(\mathbf{r},t) = -\frac{e}{4\pi}\frac{\gamma v(y-h)}{d^3(\mathbf{r},t)}, \tag{1}$$

where $\gamma = 1/\sqrt{1-\beta^2}$ is the Lorentz factor, and $d(\mathbf{r},t) = \sqrt{\gamma^2(x-vt)^2+(y-h)^2+z^2}$. It is convenient to expand the field components as a superposition of cylindrical waves, that is,

$$\begin{aligned}\tilde{E}_z^{(p)}(\mathbf{r},t) &= \mathcal{F}\big\{E_z^{(p)}(\rho,n,k_z,\omega)\big\},\\ \tilde{H}_z^{(p)}(\mathbf{r},t) &= \mathcal{F}\big\{H_z^{(p)}(\rho,n,k_z,\omega)\big\},\end{aligned} \tag{2}$$

with the operator defined as

$$\mathcal{F}(n,k_z,\omega) \equiv \sum_{n=-\infty}^{\infty}\int_{-\infty}^{\infty}dk_z\int_{-\infty}^{\infty}d\omega e^{j\omega t-jk_z z-jn\phi} \tag{3}$$

being the corresponding Fourier expansion operator. Explicit expressions for $E_z^{(p)}$ and $H_z^{(p)}$ are derived in Appendix A. The remaining components of the primary fields, namely, the radial (ρ) and azimuthal (ϕ) components, are retrieved from the longitudinal components using Maxwell's equations. In Fourier space, the following components read

$$\begin{aligned}E_\rho^{(p)} &= k_{\rm vac}^{-2}\left(jk_z\partial_\rho E_z^{(p)} + \frac{\omega\mu_0 n}{\rho}H_z^{(p)}\right),\\ E_\phi^{(p)} &= k_{\rm vac}^{-2}\left(\frac{nk_z}{\rho}E_z^{(p)} - j\omega\mu_0\partial_\rho H_z^{(p)}\right),\\ H_\rho^{(p)} &= k_{\rm vac}^{-2}\left(-\frac{\omega\varepsilon_0 n}{\rho}E_z^{(p)} + jk_z\partial_\rho H_z^{(p)}\right),\\ H_\phi^{(p)} &= k_{\rm vac}^{-2}\left(j\omega\varepsilon_0\partial_\rho E_z^{(p)} + \frac{nk_z}{\rho}H_z^{(p)}\right),\end{aligned} \tag{4}$$

where $k_{\rm vac}^2 \equiv k_z^2 - \omega^2/c^2$, and ∂_ρ denotes the derivative with respect to the radial coordinate ρ.

We now address the secondary fields (superscript "sec"), generated by the dielectric cylinder in reaction to the primary fields: The components of the secondary fields obey the homogeneous wave equation both inside the cylinder ($\rho < R$) and in the surrounding vacuum ($\rho > R$). Specifically, for the longitudinal components we have

$$\begin{aligned}\left[\nabla^2 - \varepsilon_r(\rho)\frac{1}{c^2}\frac{\partial^2}{\partial t^2}\right]\tilde{E}_z^{(\rm sec)}(\mathbf{r},t) &= 0,\\ \left[\nabla^2 - \varepsilon_r(\rho)\frac{1}{c^2}\frac{\partial^2}{\partial t^2}\right]\tilde{H}_z^{(\rm sec)}(\mathbf{r},t) &= 0,\end{aligned} \tag{5}$$

where the radial dependence of the relative permittivity in the presence of the cylinder is $\varepsilon_r(\rho < R) = \varepsilon_r$ and $\varepsilon_r(\rho > R) = 1$. The discontinuous jump in ε_r at the interface between the media ($\rho = R$) requires solving Eqs. (5) for each region separately and imposing continuity of the tangential field components.

The general solutions for Eqs. (5), which do not diverge at $\rho \to 0$ and ∞, are given in Fourier space by

$$\begin{aligned}E_z^{(\rm sec)}(\rho) &= \begin{cases}A_n(k_z,\omega)I_n(k_{\rm cyl}\rho), & \rho < R\\ B_n(k_z,\omega)K_n(k_{\rm vac}\rho), & \rho > R\end{cases},\\ H_z^{(\rm sec)}(\rho) &= \begin{cases}C_n(k_z,\omega)I_n(k_{\rm cyl}\rho), & \rho < R\\ D_n(k_z,\omega)K_n(k_{\rm vac}\rho), & \rho > R\end{cases},\end{aligned} \tag{6}$$

where $k_{\rm cyl}^2 \equiv k_z^2 - \varepsilon_r\omega^2/c^2$, and the functions $I_n(\zeta)$ and $K_n(\xi)$ are the modified Bessel functions of the first and second kind, respectively. From considerations of causality, the imaginary parts of $k_{\rm cyl}$ and $k_{\rm vac}$ are chosen to have the same sign as ω. For convenience, we henceforth omit the k_z and ω arguments from the coefficients $A_n(k_z,\omega),\ldots,D_n(k_z,\omega)$. As in Eqs. (4), the radial and azimuthal components of the secondary fields are retrieved using Maxwell's equations, yielding in Fourier space

$$\begin{aligned}E_\rho^{(\rm sec)} &= \begin{cases}k_{\rm cyl}^{-2}\big(jk_zk_{\rm cyl}A_n\dot{I}_n + \frac{\omega\mu_0 n}{\rho}C_nI_n\big) & \rho < R\\ k_{\rm vac}^{-2}\big(jk_zk_{\rm vac}B_n\dot{K}_n + \frac{\omega\mu_0 n}{\rho}D_nK_n\big) & \rho > R\end{cases},\\ E_\phi^{(\rm sec)} &= \begin{cases}k_{\rm cyl}^{-2}\big(\frac{nk_z}{\rho}A_nI_n - j\omega\mu_0k_{\rm cyl}C_n\dot{I}_n\big) & \rho < R\\ k_{\rm vac}^{-2}\big(\frac{nk_z}{\rho}B_nK_n - j\omega\mu_0k_{\rm vac}D_n\dot{K}_n\big) & \rho > R\end{cases},\\ H_\rho^{(\rm sec)} &= \begin{cases}k_{\rm cyl}^{-2}\big(-\frac{\omega\varepsilon_0\varepsilon_r n}{\rho}A_nI_n + jk_zk_{\rm cyl}C_n\dot{I}_n\big) & \rho < R\\ k_{\rm vac}^{-2}\big(-\frac{\omega\varepsilon_0 n}{\rho}B_nK_n + jk_zk_{\rm vac}D_n\dot{K}_n\big) & \rho > R\end{cases},\\ H_\phi^{(\rm sec)} &= \begin{cases}k_{\rm cyl}^{-2}\big(j\omega\varepsilon_0\varepsilon_rk_{\rm cyl}A_n\dot{I}_n + \frac{nk_z}{\rho}C_nI_n\big) & \rho < R\\ k_{\rm vac}^{-2}\big(j\omega\varepsilon_0k_{\rm vac}B_n\dot{K}_n + \frac{nk_z}{\rho}D_nK_n\big) & \rho > R\end{cases},\end{aligned} \tag{7}$$

where we denote $\dot{I}_n(\zeta)$ and $\dot{K}_n(\xi)$ as the derivatives of $I_n \equiv I_n(\zeta)$ and $K_n \equiv K_n(\xi)$, respectively. At this point it is convenient to introduce the normalized quantities $\bar{\omega} \equiv \omega R/c$ and $\bar{k} \equiv kR$ with $k \in \{k_z, k_{\rm cyl}, k_{\rm vac}\}$.

The explicit values of the coefficients $A_n, B_n, C_n,$ and D_n are retrieved by imposing boundary conditions. Since there are no free surface currents on the interface between the media ($\rho = R$), the boundary conditions are given by continuity of the field components tangential to the cylinder, namely,

$$[X^{(p)} + X^{(\rm sec)}]_{\rho=R+0} = [X^{(\rm sec)}]_{\rho=R-0}, \tag{8}$$

where $X \in \{E_\rho, E_\phi, H_\rho, H_\phi\}$. Using the orthogonality of the Fourier harmonics $\{e^{j(\omega t-n\phi-k_zz)}\}_{\omega,n,k_z}$ on the cylindrical surface satisfying $\rho = R$, the relations in Eq. (8) reduce into a linear equation system for A_n and C_n, given in matrix form by

$$\begin{pmatrix}M_{11} & M_{12}\\ M_{21} & M_{22}\end{pmatrix}\begin{pmatrix}A\\ \eta_0C\end{pmatrix} = \begin{pmatrix}\eta_0H_\phi^{(\rm eff)}\\ E_\phi^{(\rm eff)}\end{pmatrix}, \tag{9}$$

where the matrix terms read

$$\begin{aligned}M_{11} &= j\bar{\omega}\left(\varepsilon_r\frac{\dot{I}_n}{\bar{k}_{\rm cyl}} - \frac{\dot{K}_n}{K_n}\frac{I_n}{\bar{k}_{\rm vac}}\right),\\ M_{12} = M_{21} &= n\bar{k}_z\left(\frac{1}{\bar{k}_{\rm cyl}^2} - \frac{1}{\bar{k}_{\rm vac}^2}\right)I_n,\\ M_{22} &= -j\bar{\omega}\left(\frac{\dot{I}_n}{\bar{k}_{\rm cyl}} - \frac{\dot{K}_n}{K_n}\frac{I_n}{\bar{k}_{\rm vac}}\right),\end{aligned} \tag{10}$$

where now $I_n \equiv I_n(k_{\rm cyl}R)$ and $K_n \equiv K_n(k_{\rm vac}R)$, and we further define

$$\begin{aligned}E_\phi^{(\rm eff)} &= E_\phi^{(p)} - \frac{n\bar{k}_z}{\bar{k}_{\rm vac}^2}E_z^{(p)} + j\frac{\bar{\omega}}{\bar{k}_{\rm vac}}\frac{\dot{K}_n}{K_n}\eta_0H_z^{(p)},\\ \eta_0H_\phi^{(\rm eff)} &= \eta_0H_\phi^{(p)} - \frac{n\bar{k}_z}{\bar{k}_{\rm vac}^2}\eta_0H_z^{(p)} - j\frac{\bar{\omega}}{\bar{k}_{\rm vac}}\frac{\dot{K}_n}{K_n}E_z^{(p)},\end{aligned} \tag{11}$$

where η_0 is the free-space wave impedance. Inverting the matrix for each value of $n, k_z,$ and ω yields the solution for the coefficients A_n and C_n:

$$\begin{pmatrix} A_n \\ \eta_0 C_n \end{pmatrix} = \frac{1}{\Delta}\begin{pmatrix} M_{22} & -M_{12} \\ -M_{21} & M_{11} \end{pmatrix}\begin{pmatrix} \eta_0 H_\phi^{(\mathrm{eff})} \\ E_\phi^{(\mathrm{eff})} \end{pmatrix}, \tag{12}$$

where

$$\begin{aligned} \Delta = \Delta_n(\bar{k}_z, \bar{\omega}) &\equiv M_{11}M_{22} - M_{12}M_{21} \\ &= \bar{\omega}^2\left(\varepsilon_r \frac{\dot{I}_n}{\bar{k}_{\mathrm{cyl}}} - \frac{\dot{K}_n}{K_n}\frac{I_n}{\bar{k}_{\mathrm{vac}}}\right)\left(\frac{\dot{I}_n}{\bar{k}_{\mathrm{cyl}}} - \frac{\dot{K}_n}{K_n}\frac{I_n}{\bar{k}_{\mathrm{vac}}}\right) \\ &\quad - n^2\bar{k}_z^2\left(\frac{1}{\bar{k}_{\mathrm{cyl}}^2} - \frac{1}{\bar{k}_{\mathrm{vac}}^2}\right)^2 I_n^2 \end{aligned} \tag{13}$$

is the matrix determinant. The remaining coefficients B_n and D_n are found by substituting A_n and C_n into the boundary conditions for the longitudinal components in Eq. (8), yielding $B_n = K_n^{-1}(A_n I_n - E_z^{(p)})$ and $D_n = K_n^{-1}(C_n I_n - H_z^{(p)})$. Consequently, (A, B, C, D) constitutes an analytical solution for the electromagnetic fields in Fourier space, in terms of the variables $n, \bar{k}_z,$ and $\bar{\omega}$.

Observing the general expressions for the secondary fields in Eqs. (6), and the determinant in Eq. (13), we can identify three regimes in the coordinate space (k_z, ω), corresponding to waves of qualitatively different nature.

(1) $k_z^2 < \omega^2/c^2$. This regime contains radially propagating waves, contributing to the *scattered* radiation. Here both k_{cyl} and k_{vac} are imaginary, thus both $I_n(k_{\mathrm{cyl}}\rho)$ and $K_n(k_{\mathrm{vac}}\rho)$ are oscillatory.

(2) $\omega^2/c^2 < k_z^2 < \varepsilon_r\omega^2/c^2$. This regime contains the zeros of the determinant, corresponding to the dielectric cylinder's *guided* modes. These modes are mostly confined to the cylinder and carry energy in the axial (z) direction. Here k_{cyl} is imaginary but k_{cyl} is real, thus $I_n(k_{\mathrm{cyl}}\rho)$ is oscillatory and $K_n(k_{\mathrm{vac}}\rho)$ behaves asymptotically ($\rho \to \infty$) as a decaying exponential.

(3) $k_z^2 > \varepsilon_r\omega^2/c^2$. Waves in this regime are *purely evanescent*, as they both decay exponentially in the radial direction and cannot be guided by the cylindrical structure. Therefore, these waves do not contribute to the emitted radiation and are thus not considered in this paper.

B. Scattered radiation

With the coefficients characterizing the electromagnetic fields emitted by the system at hand [see Eq. (12)], the radially emitted energy by these propagating modes can now be calculated. The scattered energy is determined by integrating the *radial* component of the Poynting vector corresponding to the secondary field, $\tilde{S}_\rho^{(\mathrm{sec})} = \tilde{E}_\phi^{(\mathrm{sec})}\tilde{H}_z^{(\mathrm{sec})} - \tilde{E}_z^{(\mathrm{sec})}\tilde{H}_\phi^{(\mathrm{sec})}$, over a cylindrical surface of radius ρ with the same axis as the dielectric rod, and taking the limit $\rho \to \infty$. The first term corresponds to the transverse electric (TE) contribution, whereas the second is the transverse magnetic (TM) counterpart. Explicitly, the emitted energy W_{scat} is given by

$$W_{\mathrm{scat}} = \lim_{\rho\to\infty} \rho \int_{-\infty}^{\infty} dt \int_{-\infty}^{\infty} dz \int_{-\pi}^{\pi} d\phi \times \left(\tilde{E}_\phi^{(\mathrm{sec})}\tilde{H}_z^{(\mathrm{sec})} - \tilde{E}_z^{(\mathrm{sec})}\tilde{H}_\phi^{(\mathrm{sec})}\right). \tag{14}$$

Using Parseval's identity and the large-argument asymptotic expansions for the modified Bessel functions [29], we get the following expression for the normalized scattered energy:

$$\begin{aligned} \bar{W}_{\mathrm{scat}} &\equiv \frac{W_{\mathrm{scat}}}{(e^2/4\pi\varepsilon_0 R)} \\ &= \frac{1}{2}(2\pi)^3 \int_0^\infty d\bar{\omega}\bar{\omega} \sum_{n=-\infty}^{\infty} \int_0^{\bar{\omega}} d\bar{k}_z \frac{1}{\bar{\omega}^2 - \bar{k}_z^2} \\ &\quad \times [|\hat{B}_n(\bar{k}_z, \bar{\omega})|^2 + |\hat{D}_n(\bar{k}_z, \bar{\omega})|^2], \end{aligned} \tag{15}$$

where $\hat{B}_n = B_n(\frac{e}{4\pi}\eta_0)^{-1}$, $\hat{D}_n = D_n(\frac{e}{4\pi})^{-1}$, and the terms $|\hat{D}_n(\bar{k}_z, \bar{\omega})|^2$ and $|\hat{B}_n(\bar{k}_z, \bar{\omega})|^2$ in the integrand are associated with the TM and TE term, respectively. A detailed derivation of Eq. (15) is presented in Appendix B. The integrand of Eq. (15) yields the normalized spectrum:

$$\frac{d\bar{W}_{\mathrm{scat}}}{d\bar{\omega}} = \frac{1}{2}(2\pi)^3\bar{\omega} \sum_{n=-\infty}^{\infty} \int_0^{\bar{\omega}} d\bar{k}_z \frac{1}{\bar{\omega}^2 - \bar{k}_z^2} \times [|\hat{B}_n(\bar{k}_z, \bar{\omega})|^2 + |\hat{D}_n(\bar{k}_z, \bar{\omega})|^2]. \tag{16}$$

The integration of $\bar{k}_z$ in Eqs. (15) and (16) accounts only for the radially propagating waves, $\bar{k}_z^2 < \bar{\omega}^2$, as they are the sole contributors to the scattered radiation. In addition, the matrix is invertible (i.e., nonzero determinant) for every value of $\bar{k}_z$ and $\bar{\omega}$ in this region, ensuring $B_n(\bar{k}_z, \bar{\omega})$ and $D_n(\bar{k}_z, \bar{\omega})$ have converging values.

C. Guided radiation

In addition to radially scattered waves, the electron's evanescent fields also excite the cylinder's guided modes, which in turn carry energy W_{guided} in both axial (z) directions equally, thus the factor 2 in the explicit expression

$$W_{\mathrm{guided}} = 2 \times \lim_{z\to\infty} \int_{-\infty}^{\infty} dt \int_0^{\infty} d\rho\rho \int_{-\pi}^{\pi} d\phi \times \left(\tilde{E}_\rho^{(\mathrm{sec})}\tilde{H}_\phi^{(\mathrm{sec})} - \tilde{E}_\phi^{(\mathrm{sec})}\tilde{H}_\rho^{(\mathrm{sec})}\right). \tag{17}$$

In the integrand we may identify the *longitudinal* component of the Poynting vector $\tilde{S}_z = \tilde{E}_\rho^{(\mathrm{sec})}\tilde{H}_\phi^{(\mathrm{sec})} - \tilde{E}_\phi^{(\mathrm{sec})}\tilde{H}_\rho^{(\mathrm{sec})}$. The various integrals may be performed analytically in the Fourier domain by employing the orthogonality of the various eigenfunctions, as well as the Cauchy residue theorem. The detailed process is long and tedious and it does not contribute to the understanding of the physics process involved. For this reason, in the remainder of this subsection we highlight the main steps of our analysis, whereas the details are presented in Appendix C.

As a first step, each one of the space- and time-domain field components $(\tilde{E}_\rho^{(\mathrm{sec})}, \tilde{H}_\phi^{(\mathrm{sec})}, \tilde{E}_\phi^{(\mathrm{sec})}, \tilde{H}_\rho^{(\mathrm{sec})})$ is converted into the Fourier domain. The corresponding functions may be formally expressed as

$$\begin{aligned} X(\bar{z}) &= \int_{-\infty}^{\infty} d\bar{k}_z \frac{\bar{X}(\bar{k}_z)}{\Delta(\bar{k}_z)} e^{-j\bar{k}_z\bar{z}} \\ &= \sum_{s=1}^{\infty} \bar{X}(\bar{k}_{n,s}) \qquad (18) \\ &\quad \times \int_{-\infty}^{\infty} d\bar{k}_z \frac{e^{-j\bar{k}_z\bar{z}}}{\Delta(\bar{k}_z = \bar{k}_{n,s}) + \left(\bar{k}_z^2 - \bar{k}_{n,s}^2\right)\left[\frac{\partial\Delta}{\partial\bar{k}_z^2}\right]_{\bar{k}_z^2=\bar{k}_{n,s}^2}} \\ &= \sum_{s=1}^{\infty} 2\bar{k}_{n,s} \frac{\bar{X}(\bar{k}_{n,s})}{\dot{\Delta}_{n,s}} \int_{-\infty}^{\infty} d\bar{k}_z \frac{e^{-j\bar{k}_z\bar{z}}}{\bar{k}_z^2 - \bar{k}_{n,s}^2} \qquad (19) \end{aligned}$$

whose main contributions come from the zeros of the determinant $\Delta(\bar{k}_z = \bar{k}_s) \equiv 0$; $s = 1, 2, \dots, \infty$ represents the radial index of the eigenmode, and in what follows we denote the first derivative of the determinant as $\dot{\Delta}_{n,s} \equiv [\partial\Delta/\partial\bar{k}_z]_{\bar{k}_z=\bar{k}_{n,s}}$. Note that dependence on the normalized frequency ($\bar{\omega}$) is hidden in this notation.

As mentioned above, these roots lie strictly in the range $\bar{\omega} < \bar{k}_z < \sqrt{\varepsilon_r}\bar{\omega}$, indicating that the fields of the corresponding modes oscillate in the cylinder's interior and decay exponentially in its exterior. In addition, for any given value of the variables n, $\bar{k}_z$, and $\bar{\omega}$, and obviously for s, the various modes (for different radial indices) form an orthonormal set with respect to the following orthogonality relation [30]:

$$\int_0^{\infty} d\rho\rho[\mathcal{E}_{\rho,s}\mathcal{H}_{\phi,s'}^* - \mathcal{E}_{\phi,s}\mathcal{H}_{\rho,s'}^*](\rho) = \delta_{s,s'}, \qquad (20)$$

where $\delta_{s,s'}$ is the Kronecker delta function. The calligraphic terms represent the corresponding field components satisfying the corresponding boundary conditions with one difference: the amplitude is chosen such that the diagonal terms are unity.

The next step is to use Cauchy's residue theorem, as well as the various modes' orthogonality, to express the normalized energy carried by the guided modes,

$$\begin{aligned} \bar{W}_{\text{guided}} &\equiv \frac{W_{\text{guided}}}{e^2/4\pi\varepsilon_0 R} \\ &= \frac{1}{2}(4\pi)^3 \int_0^{\infty} d\bar{\omega} \sum_{n=-\infty}^{\infty} \sum_{s=1}^{\infty} \frac{1}{\dot{\Delta}_{n,s}^2} \\ &\quad \times \text{Re}\left\{\int_0^{\infty} d\bar{\rho}\bar{\rho}[\hat{E}_\rho\hat{H}_\phi^* - \hat{E}_\phi\hat{H}_\rho^*]_{\bar{k}_z=\bar{k}_{n,s}}\right\}, \qquad (21) \end{aligned}$$

where $\hat{E}_\nu$ and $\hat{H}_\nu$ are the nondimensionalized field components normalized by the determinant, given by the following relations:

$$\begin{aligned} E_\nu^{(\text{sec})} &= \frac{e}{4\pi}\eta_0\frac{\hat{E}_\nu}{\Delta_n}, \\ H_\nu^{(\text{sec})} &= \frac{e}{4\pi}\frac{\hat{H}_\nu}{\Delta_n}, \qquad \nu \in \{\rho, \phi\}. \qquad (22) \end{aligned}$$

Consequently, the guided waves' spectrum is determined by

$$\begin{aligned} \frac{d\bar{W}_{\text{guided}}}{d\bar{\omega}} &= \frac{1}{2}(4\pi)^3 \sum_{n=-\infty}^{\infty} \sum_{s=1}^{\infty} \frac{1}{\dot{\Delta}_{n,s}^2} \\ &\quad \times \text{Re}\left\{\int_0^{\infty} d\bar{\rho}\bar{\rho}[\hat{E}_\rho\hat{H}_\phi^* - \hat{E}_\phi\hat{H}_\rho^*]_{\bar{k}_z=\bar{k}_{n,s}}\right\}. \qquad (23) \end{aligned}$$

The expressions for the guided energy [Eq. (22)] and spectrum [Eq. (23)], together with their scattered equivalents [Eqs. (15) and (16), respectively], provide a complete description of the radiation emitted following the point particle's motion in the vicinity of the dielectric rod. By conservation of energy, the sum of energy radiated by the scattered and guided waves is equal to the work done on the particle by the decelerating force exerted by the secondary fields. In addition to deceleration, the secondary fields also apply a transverse kick, deflecting the particle from its original, straight trajectory (in the x direction). The change in momentum due to the transverse kick has been characterized for a line source in Ref. [22], but is omitted from this paper due to space considerations.

In the section that follows, the aforementioned quantities will be evaluated and their dependence on the system parameters will be considered.

III. NUMERICAL ANALYSIS

In this section we employ the analytic formulation developed in the previous section to assess numerically the integral expressions for the energy radiated in the system by the radially scattered waves [Eq. (15)] and the guided modes [Eq. (22)], as well as their respective frequency spectra [Eqs. (16) and (23)]. The dependence of these quantities is examined with respect to the following parameters which characterize the system: For convenience, from now on $\gamma - 1$ will be referred to as "kinetic energy," or simply "energy." Since all length quantities can be normalized with respect to the cylinder's radius R, the radius itself is not an additional independent parameter in the problem. We denote the ratio between the electron's impact parameter and R as $\eta = h/R$.

Typical scales of interest for the system's parameters are now addressed. Considered values of ε_r lie inside the range $2 \leqslant \varepsilon_r \leqslant 12$, as it covers the dielectric coefficients of most materials used in optical fibers and optical acceleration structures. For instance, a typical value for the relative permittivity of fused silica (SiO_2) is $\varepsilon_r \approx 2.1$ and that of silicon (Si) is $\varepsilon_r \approx 12.1$ [31]. We consider in our investigation both low but moderately relativistic energies ($0.01 < \gamma - 1 < 1$), as present in electron microscopes, and high ultrarelativistic energies ($\gamma - 1 \gg 1$) that are relevant to optical accelerators. Below $\gamma - 1 = 0.01$ the cylinder's response can be safely considered quasistatic, with both scattered and guided radiation being negligible, therefore no special attention is paid towards this regime.

An additional characteristic value of interest is the cylinder's Čerenkov velocity, $\beta_c = 1/\sqrt{\varepsilon_r}$, which is the phase velocity of light inside the dielectric medium. The corresponding Čerenkov energy is defined as $\gamma_c - 1 = 1/\sqrt{1 - \beta_c^2} - 1$. Analyzing the behavior of the scattered and guided radiation for energies below and above $\gamma_c - 1$ allows us to determine if there exists any qualitative difference between "pure" and "Čerenkov-assisted" scattered or guided radiation.

A. Preliminary assumption: Frequency-dependent permittivity

In the idealistic formulation of the problem, the cylinder has a constant relative permittivity ε_r over all frequencies.

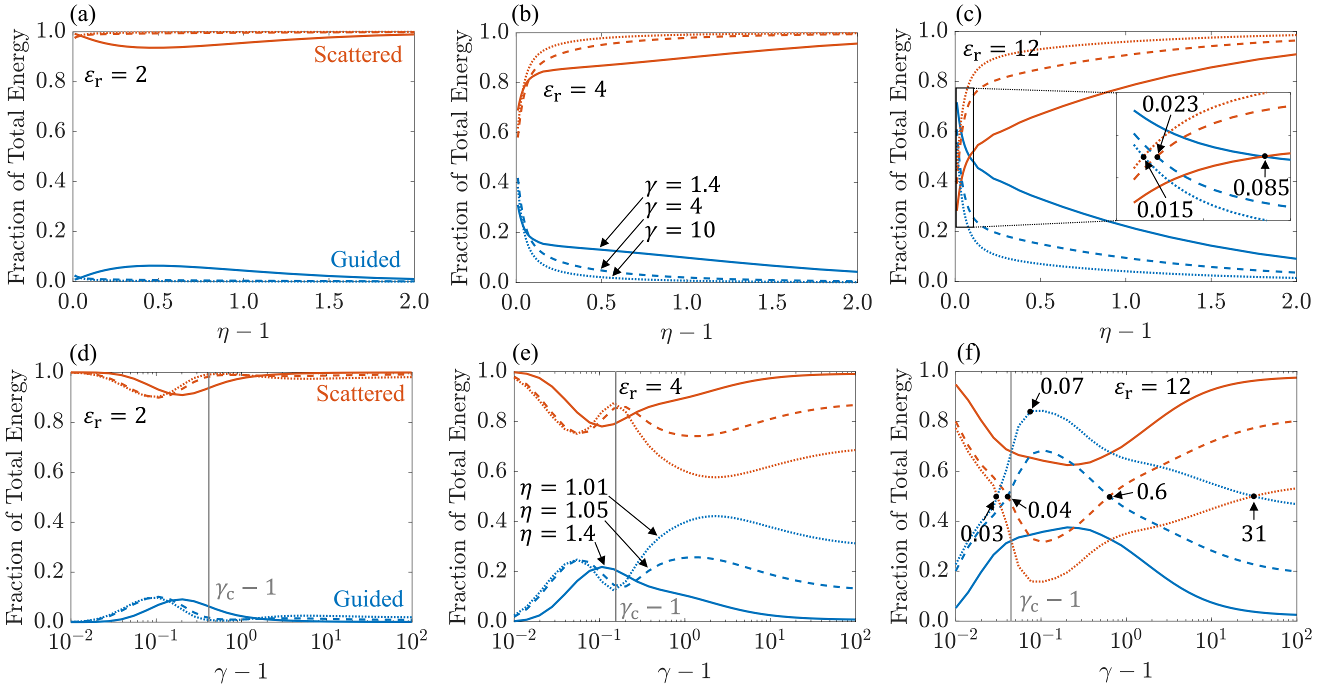

FIG. 2. Comparison between the scattered and guided energies normalized to total energy. (a–c) Normalized scattered and guided energies vs normalized distance from the cylinder ($\eta - 1$) for multiple kinetic energies, plotted for (d) $\varepsilon_r = 2$, (e) $\varepsilon_r = 4$, and (f) $\varepsilon_r = 12$. The inset in panel (c) zooms on the range $0 < \eta - 1 < 0.1$ and distances below which the guided energy becomes dominant are marked on it. (d)–(f) Normalized scattered and guided energies vs kinetic energy ($\gamma - 1$) for multiple distances from the cylinder, plotted for (a) $\varepsilon_r = 2$, (b) $\varepsilon_r = 4$, and (c) $\varepsilon_r = 12$. The Ĉerenkov energy $\gamma_c - 1$ for each permittivity is denoted as a reference value. Energies where the scattered and guided energy curves intersect and the maximal peak location for the guided energy are marked in panel (c).

However, from convergence considerations it is assumed in the analysis that follows that the permittivity drops down to 1 above a certain "cutoff frequency" ω_{co}, expressed in normalized frequencies by

$$\varepsilon_r(\bar{\omega}) = \begin{cases} \varepsilon_r, & \bar{\omega} < \bar{\omega}_{\text{co}} \\ 1, & \bar{\omega} > \bar{\omega}_{\text{co}} \end{cases}. \tag{24}$$

The following simplifies computations by requiring us to integrate in frequency only up to $\bar{\omega}_{\text{co}}$ instead of up to infinity, as modes with frequencies exceeding $\bar{\omega}_{\text{co}}$ "see" vacuum rather than a cylindrical obstacle.

In order to assign a physically reasonable value to $\bar{\omega}_{\text{co}}$, we note that most materials relevant to optical fibers and optical acceleration structures (with the exception of fused quartz) are essentially transparent in the far UV, namely, for wavelengths below 200 nm [31]. Assuming a lower threshold of $\lambda_{\text{co}} = 200$ nm for the wavelength and a cylinder radius of $R = 1\ \mu$m (typical for optical structures) yields a normalized cutoff frequency of $\bar{\omega}_{\text{co}} = 10\pi$. It was numerically verified that, following this assumption, taking azimuthal harmonics in the range $-40 \leqslant n \leqslant 40$ and radial harmonics in the range $1 \leqslant s \leqslant 40$ (in the case of guided radiation) inside the summations is sufficient for convergence. More details regarding the convergence of our numerical computations and the incorporation of losses are presented in Appendix H and I. Beyond the dependence specified in Eq. (24), the dielectric coefficient of the material is assumed to be frequency independent, ignoring the various resonances of the material(s) involved.

B. Radiated energy comparison

We begin by comparing between the energy emitted in the form of scattered waves, W_{scat}, and that carried by guided modes, W_{guided}, as a function of ε_r, η, and $\gamma - 1$. It is insightful to plot the relative portion of each energy type out of the total emitted energy $W_{\text{total}} = W_{\text{scat}} + W_{\text{guided}}$ rather than their separate values, as presented in Fig. 2. From Figs. 2(a)–2(c) it can be seen that for large distances from the cylinder ($\eta \gg 1$) the scattered energy is clearly the dominant contribution to the emitted energy. However, for small distances ($\eta \approx 1$) the picture is slightly more complex: For low permittivities the scattered energy remains dominant, but, as permittivity increases, the contribution of guided modes becomes more significant and can even exceed that of the scattered waves, as depicted in Fig. 2(f). This suggests that mode excitation inside the cylinder by the point particle's evanescent fields is significant only for cylinders with large dielectric coefficients and in the case that the particle "grazes" the cylinder's surface. The following is in agreement with the fact that the cylinders with larger ε_r support more guided modes for any given frequency, and that a smaller impact parameter leads to stronger evanescent fields impinging the rod during the particle's approach. However, the latter also applies to the scattered radiation, making the stronger dependence of the guided energy in η a nontrivial result.

Figures 2(d)–2(f) reveal that the guided energy is most significant for moderately relativistic energies (roughly $10^{-1} < \gamma - 1 < 10^1$ in orders of magnitude) and gradually becomes less apparent as energy increases or alternatively approaches

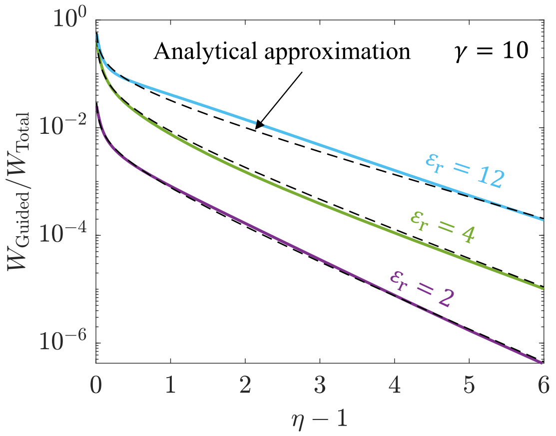

FIG. 3. Analytical approximation of the guided energy normalized to total energy. The colored solid lines are numerical plots of the normalized guided energy (in log scale) vs normalized distance from the cylinder ($\eta - 1$) for $\gamma = 10$ and multiple permittivities, and the black dashed lines are the corresponding analytical fits based on Eq. (25), yielding a decent approximation.

the quasistatic limit, yet the exact energy range strongly depends on the choice of η and ε_r. To quote some concrete examples, the guided energy constitutes more than 20% of the total energy in the ranges $0.04 < \gamma - 1 < 0.1$ and $0.4 < \gamma - 1 < 8$ for $\varepsilon_r = 4$ and $\eta = 1.05$, and in the range $0.2 < \gamma - 1 < 2$ for $\varepsilon_r = 12$ and $\eta = 2$. For sufficiently large permittivities and small enough distances, the guided energy can remain comparable to the scattered energy even for ultrarelativistic energies, as observed for $\varepsilon_r = 12$ and $\eta = 1.01$. From a practical perspective, the following results indicate that guided mode excitation can be significant in electron microscopy systems characterized by low electron energies (order of 100 keV), whereas in optical acceleration structures characterized by higher energies (order of 10 MeV) the leading contribution to the wakefield comes from the scattered waves, as long as the electron does not graze the structure. It is also observed that the energies where the guided mode contribution reaches its maximum lie in most cases in the vicinity of the Čerenkov energy, differing by no more than a single order of magnitude. This indicates a possible relation between mode excitation and a Čerenkov-like mechanism for the emission of radiation in this form, as was shown in previously considered configurations [20,32].

Since the exact expressions for the energy components are not given in closed form and require long computation times to evaluate, obtaining analytical expressions for the following quantities is of great importance, as they provide useful scaling laws with minimal computational effort. Most normalized energy curves illustrated in Fig. 3 exhibit complicated behavior, yet for the case of $\gamma = 10$ a rough analytical approximation for the relative portion of the guided energy was found, taking the following form:

$$\frac{W_{\text{guided}}}{W_{\text{total}}} \approx c_1 \frac{e^{-c_2(\eta-1)}}{(\eta-1)^{c_3}}, \tag{25}$$

where $c_1, c_2,$ and c_3 are constants dependent on ε_r and $\gamma - 1$. Plots of the analytical fit compared to the numerical computation for $\gamma = 10$ and multiple permittivities are presented in Fig. 3, yielding a decent approximation (relative integrated square error of less than 3%) in the range $0.01 < \eta - 1 < 2$. For $\varepsilon_r = 2, 4,$ and 12 the constants for the fits in Fig. 3 read, respectively, $c_1 \approx 0.003, 0.026,$ and 0.075; $c_2 \approx 1.31, 1.10,$ and 0.86; and $c_3 \approx 0.51, 0.65,$ and 0.45. The overall amplitude c_1 is observed to roughly scale linearly with ε_r and the decay rate c_2 decreases with ε_r, demonstrating the strong ε_r dependence of the guided energy's relative portion. In general, the following approximation exemplifies the strong η dependence of the guided radiation's relative contribution and shows that it decays exponentially with the distance (divided by a power). This approximation breaks up when considering smaller values of γ and expanding the distance range to large values of η, leading to a significant discrepancy.

C. Spectrum comparison

Our next step is to compare between the frequency spectra of the scattered and guided radiation and their dependence on the system parameters. The preceding comparison of the normalized energy portions (recall Fig. 2) allows us to identify multiple regions of interest, where plotting the corresponding spectra may reveal further insight on the various radiation types.

Plots of the scattered and guided radiation spectra in multiple regions are presented in Fig. 4. For low permittivities [Fig. 4(a)] both the scattered and guided spectra are mostly smooth, containing only a few peaks. As permittivity increases, significant quasiperiodic resonant peaks start to emerge, as seen in Fig. 4(b). These peaks are geometry dependent, as their locations depend only the cylinder's permittivity ε_r, regardless of the particle's position and energy. Resonant behavior is apparent for both scattered and guided spectra, yet the reason for their presence is fundamentally different: In the case of scattered radiation, propagating waves inside the cylinder interfere differently for different frequencies, causing certain frequencies to be scattered more significantly and other frequencies to be attenuated. The resonances in the scattered spectrum correspond to frequencies of increased scattering. On the other hand, resonances in the guided spectrum are associated with the excitation of new eigenmodes, propagating along the rod's axis.

For high energies and large impact parameters [Fig. 4(c)], the scattered radiation is much more significant than its guided counterpart, with the scattered spectrum resembling the cross section of a TE plane wave (i.e., magnetic field parallel to the cylinder's axis) scattered from an identical cylinder (see Ref. [32] pp. 79–83). The following is in accordance with the fact that the amplitude ratio of the longitudinal components of the primary field ($E_z^{(\mathrm{p})}, H_z^{(\mathrm{p})}$) approaches the free-space wave impedance, as in a plane wave. The wide resonant peaks are periodic, with the normalized distance between adjacent peaks roughly being $\Delta\bar{\omega} \sim \pi/(\sqrt{\varepsilon_r} - 1)$. On top of those wide peaks are smaller resonances, stemming from oscillations in the determinant from Eq. (13), and are more complicated to characterize. The mean spacing between these resonances is nevertheless observed to scale like $\Delta\bar{\omega} \propto 1/\sqrt{\varepsilon_r}$, which is equal to the cylinder's Čerenkov velocity. We note that the scattered spectrum in this regime also bears visual

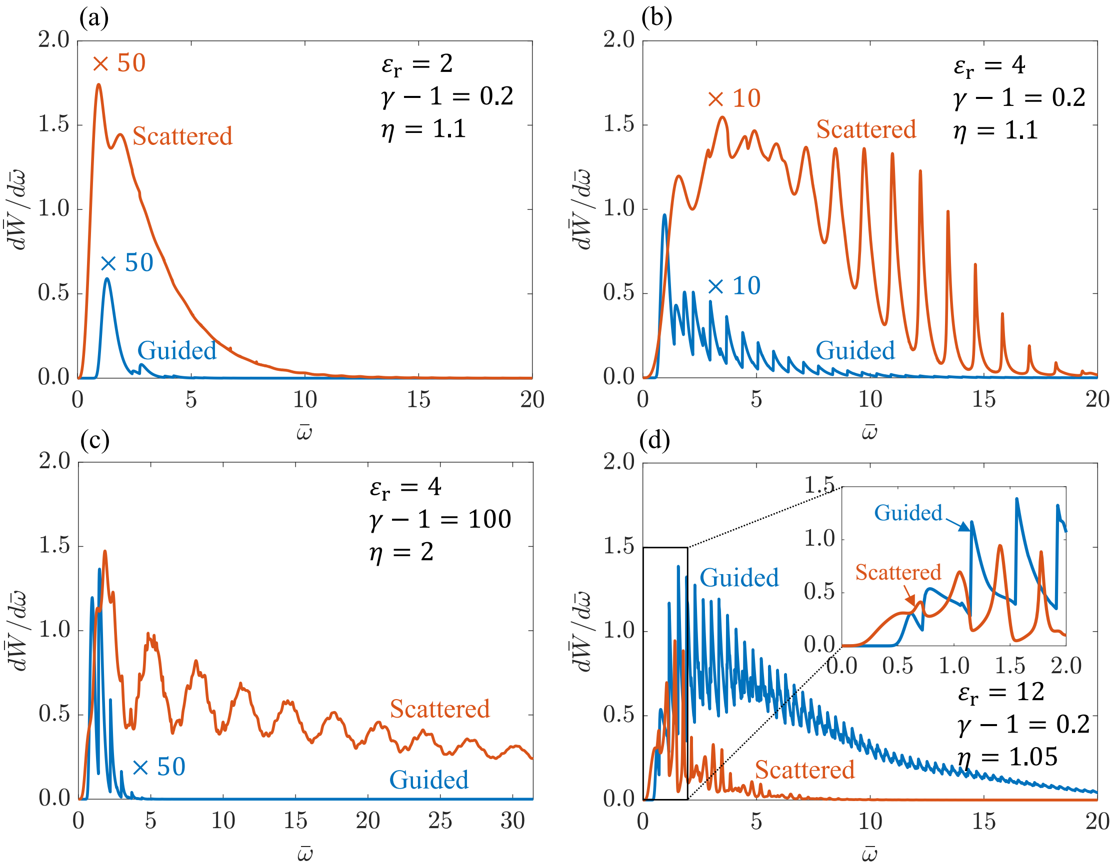

FIG. 4. Comparison between the spectra of the scattered and guided radiation. The spectra are plotted as a function of the normalized frequency $\bar{\omega} = \omega R/c$ for multiple regimes of interest: (a) small permittivity, low energy, and small distance from the cylinder (scattered radiation dominant). (b) Medium permittivity, low energy, and small distance from the cylinder (scattered radiation dominant). (c) Medium permittivity, high energy, and large distance from the cylinder (scattered radiation dominant). (d) High permittivity, low energy, and small distance from the cylinder (guided radiation dominant). The inset zooms on the range $0 \leqslant \bar{\omega} \leqslant 2$, showing "antiphase" alternation between the scattered and guided spectral peaks. Curves with small values are scaled by a multiplicative factor for clarity.

resemblance to the spectrum induced by a charged line, as studied in Ref. [22].

Figure 4(d) demonstrates that the guided radiation can become more significant than scattering in the case of a small impact parameter, low (yet relativistic) energy, and a large permittivity. An intriguing observation seen from the inset is that for low frequencies the scattered and guided spectra seem to be in "antiphase," that is, the scattered spectrum attains a local maximum roughly where the guided spectrum is at a local minimum, and vice versa. The following may be intuitively explained in the framework of conservation of energy: The particle's evanescent fields inject energy into the system (rod and vacuum), with part of it being scattered and the remainder being confined to the rod. Therefore, for frequencies with significant scattering we would expect weaker confinement to the cylinder and thus less substantial mode excitation, and vice versa.

As with the radiated energy, approximate forms and scaling laws for the frequency spectrum of both radiation types are also desired. The spectrum of the scattered radiation is addressed first. For *low energies*, an approximation of the following form was found:

$$\frac{d\bar{W}_{\text{scat}}}{d\bar{\omega}} \simeq a\left[\left(1 - \frac{1}{2}J_0^2(u) - \frac{1}{2}\text{jinc}^2(u)\right)^2\right]_{u=\eta b\bar{\omega}/\beta} \times \exp\left(-2\frac{\eta - 1}{\gamma\beta}\bar{\omega}\right), \tag{26}$$

where $\text{jinc}(u) \equiv 2J_1(u)/u$, a and b are coefficients dependent on ε_r, η, and $\gamma - 1$, and the quantity $\gamma\beta$ is proportional to the particle's relativistic momentum. The first term in the product can be thought of as the cylinder's low-frequency response. In addition, in the limit $\bar{\omega} \to 0$ this term exhibits a $\bar{\omega}^4$ dependence, similar to the fourth-power dependence present in dipole radiation and in Rayleigh scattering. The second term is a decaying exponential in $\bar{\omega}$, dictated by the particle's evanescent fields.

For *high energies*, we utilize the plane-wave scattering resemblance of the spectrum observed in Fig. 4(c) and construct

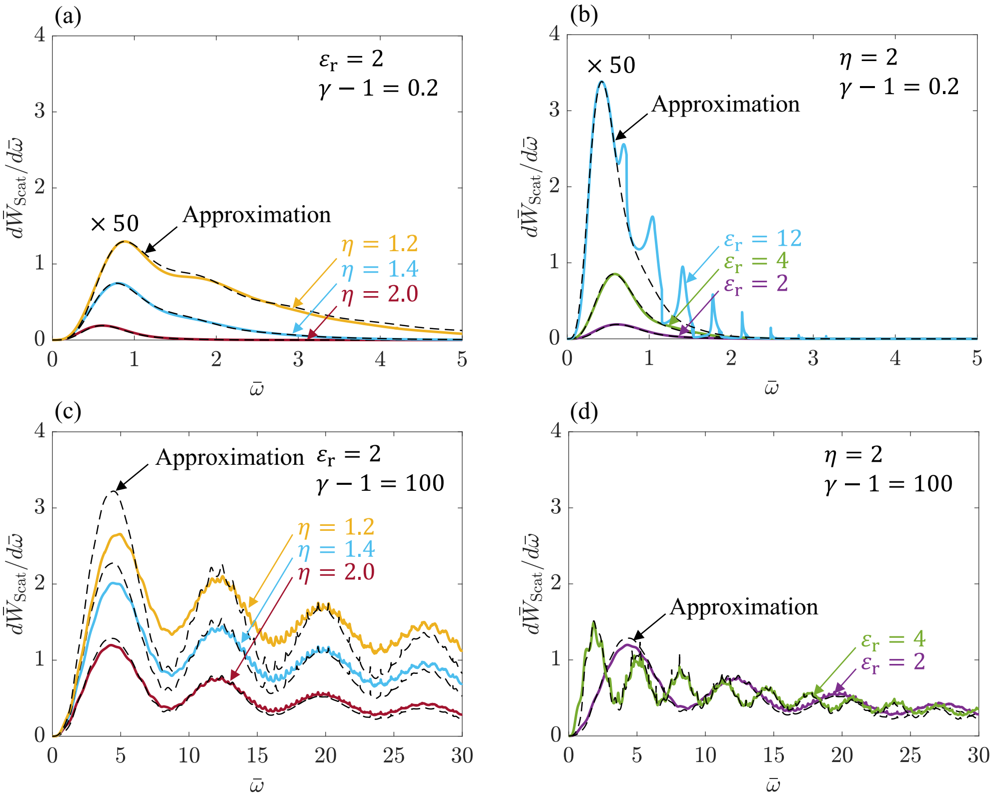

FIG. 5. Approximation for the scattered radiation spectrum. The proposed approximations (black dashed line) are compared to the numerical spectra (colored solid lines) for multiple regimes and system parameter values: (a) Low energy [based on Eq. (26)], multiple η. (b) Low energy [based on Eq. (26)], multiple ε_r. (c) High energy [based on Eq. (27)], η. (d) High energy [based on Eq. (27)], multiple ε_r. Curves with small values are scaled by a multiplicative factor for clarity.

a similar approximation as follows:

$$\frac{d\bar{W}_{\mathrm{scat}}}{d\bar{\omega}} \simeq a S^{\mathrm{TE}}_{\mathrm{Plane}}(\bar{\omega}) \times \exp\left(-2\frac{\eta}{\gamma\beta}\bar{\omega}\right), \qquad (27)$$

where $S^{\mathrm{TE}}_{\mathrm{plane}}(\bar{\omega})$ is the scattering cross section of a TE plane wave scattered from an identical cylinder, as formulated in Ref. [32] pp. 79–83. Here, substituting η inside the exponential instead of $\eta - 1$ is more appropriate, since the evanescent fields' penetration into the cylinder is more significant for high energies, reaching the cylinder's interior rather than decaying close to its surface. Therefore, choosing the particle's distance from the cylinder's axis (namely, η) is more reasonable compared to the particle's distance from the surface ($\eta - 1$).

The proposed approximations are compared to the exact, numerically evaluated spectra for multiple values of ε_r, η, and $\gamma - 1$ in Fig. 5, yielding a decent fit for values of η not too close to 1 and values of ε_r not too high. As a concrete example, for $\varepsilon_r = 2, 4,$ and 12 the constants for the fits in Fig. 5(a) read $a \simeq 0.010, 0.012,$ and 0.013 and $b \simeq 1.16, 0.84,$ and 0.75, respectively. The low-energy approximation [Eq. (26)] successfully captures both low-frequency behavior (including the first peak) and high-frequency exponential decay, but does not incorporate the geometric resonances, as witnessed in Fig. 5(b) for $\varepsilon_r = 12$. In addition, for low energies both the maximal peak's location and height strongly increase with ε_r and as η gets closer to 1. For high energies, an explicit expression for the maximal peak's approximate location can be found. By approximating the plane-wave cross section with a first-order Struve function (see Sec. 15.32 in Ref. [33]) and solving for its maximum, we obtain a simple expression for the peak location which is independent of η and γ, reading

$$\bar{\omega}_{\max} \simeq \frac{1.81}{\sqrt{\varepsilon_r} - 1}. \qquad (28)$$

Figure 5(c) shows that, similar to low energies, for high energies the maximal peak height also strongly increases as η approaches 1. Explicitly, for $\eta = 2.0$, 1.4, and 1.2 the normalization factors for the fits in this plot read $a \approx 0.81, 1.36,$ and 1.89, respectively. Figure 5(d), however, depicts a rather weak dependence of the maximal peak's height in ε_r. Practically speaking, the independence of the maximal peak's location in the particle's motion parameters (namely, $\gamma - 1$ and η) for high energies makes beam diagnostics in this regime based on the scattered spectrum a difficult task.

Further insight is obtained from comparing between the contributions of the TE and TM components of the scattered energy, as presented in Eq. (15). As it turns out, the dominant contribution comes from the TE component. For a detailed discussion about the dominance of the TE term and its origin, we refer the reader to Appendix D.

In the case of the guided radiation, the spectrum may provide insight on the radiation's modal distribution, that is, the

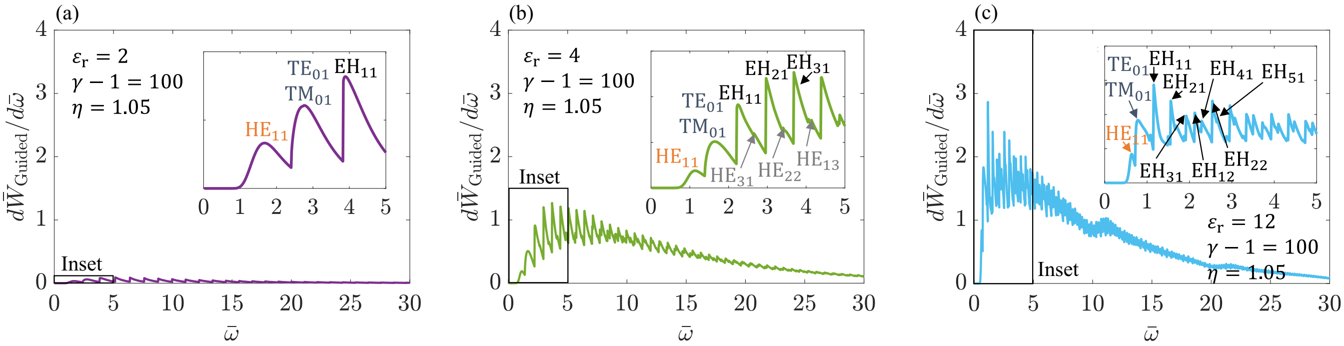

FIG. 6. Mode distribution along the guided radiation spectrum. The spectrum is plotted for $\eta = 1.05, \gamma - 1 = 100$, and multiple permittivities: (a) $\varepsilon_r = 2$, (b) $\varepsilon_r = 4$, and (c) $\varepsilon_r = 12$. The insets focus on the range $0 \leqslant \bar{\omega} \leqslant 5$ and the mode types corresponding to the first couple of peaks are denoted, demonstrating that the dominant contribution comes from the TE$_{01}$ ($n = 0, s = 1$), TM$_{01}$ ($n = 0, s = 2$), HE$_{11}$ ($n = \pm 1, s = 1$), and EH$_{nm}$ ($|n| \geqslant 1$, even s) modes. A detailed description of the conversion between our (n, s) notation and the notation common in the literature for the eigenmodes of a cylindrical dielectric waveguide is presented in Appendix G.

extent to which each cylinder eigenmode is excited following the particle's approach. As stated earlier, each resonant peak in the guided spectrum corresponds to the excitation of a specific mode. Figure 6 displays the spectrum in the case that the particle is close to the cylinder ($\eta \approx 1$) for multiple permittivities, with the corresponding mode type (as formulated in Ref. [34] p. 139) of the first few peaks being denoted. The first couple of peaks are smooth, and become gradually sharper as frequency increases, until a discontinuity appears. Therefore, the peak maximum for high frequencies is effectively at the cutoff frequency of the corresponding mode. The first peak corresponds to the 'fundamental mode," HE$_{11}$ ($n = \pm 1, s = 1$), which has no cutoff frequency. The second peak belongs to the TE$_{01}$ and TM$_{01}$ modes ($n = 0, s = 1$), which have no longitudinal electric- or magnetic-field component, respectively. It is observed that the remainder of the significant peaks are effectively contributed only by the EH$_{n\nu}$ modes ($|n| \geqslant 1$, even s), which are hybrid modes with a dominant TM component.

The following plots show that the peaks' heights remain comparable even for large azimuthal harmonics (n) for small impact parameters, indicating that a large number of modes must be considered in the analysis of the guided radiation. Moreover, this number increases with ε_r, roughly scaling as $\sqrt{\varepsilon_r - 1}$. For low permittivities it is sufficient to consider only EH modes with a radial index of $s = 1$, whereas for higher permittivities larger values of s must be taken into account.

Although the cylinder's dispersion equation $\Delta_n(\bar{\omega}, \bar{k}_z) = 0$ cannot be solved analytically, the cutoff frequencies of the TE$_{01}$, TM$_{01}$, and EH$_{nm}$ modes have simple expressions, allowing us to easily characterize the guided spectrum's significant peaks apart from the fundamental mode HE$_{11}$, whose peak is located before those of the former modes. Referring to Eqs. (5.45) and (5.48) in Ref. [34], the following cutoff frequencies, which are effectively the peaks' locations, are given by

$$\bar{\omega}_{n,m} = \frac{j_{n,m}}{\sqrt{\varepsilon_r - 1}}, \tag{29}$$

where $j_{n,m}$ is the mth root of the nth-order Bessel function, $J_n(x)$, $n = 0, 1, 2, \ldots$, and $m = 1, 2, \ldots$.

A more thorough examination, presented in Appendix E, reveals that the dominant contribution to the spectrum comes from nonpositive values of n, which correspond to nonrotating ($n = 0$) or clockwise-rotating ($n < 0$) waves for positive frequencies. The following asymmetry between positive and negative harmonics may be attributed to clockwise-rotating dipoles (for $n = -1$) or higher multiples (for $n < -1$) induced inside the cylinder by the particle's fields during its motion in the positive x direction. Such asymmetric angular content was also found to apply for the scattered radiation.

D. Effect of a finite-size bunch

The preceding analysis addresses the radiation emitted as the cylinder is impinged by the evanescent fields of a point charge, yet realistic electron beams moving inside optical accelerators have some spatial extent. To this end, we introduce a simple model for a finite-size bunch, composed of a uniform cylindrical charge distribution with an axis parallel to the x axis, and characterized by a width of $2\Delta_x$ and a radius of Δ_r. Since direct contact between the bunch and the structure is undesired, the bunch radius is constrained to satisfy $\Delta_r < h - R$. By virtue of superposition, the fields induced by the bunch are given by integrating the fields of a point particle over the entire charge distribution. For the considered bunch geometry, the superposition translates in Fourier space to multiplication by a "bunch factor," with the bunch's fields given as a function of Δ_x and Δ_r as follows:

$$\begin{aligned} X(\Delta_x, \Delta_r) &= X(\Delta_x = 0, \Delta_r = 0) \\ &\quad \times \operatorname{sinc}\left(\frac{1}{\beta}\frac{\omega}{c}\Delta_x\right) \operatorname{Iinc}\left(\frac{1}{\gamma\beta}\frac{\omega}{c}\Delta_r\right), \\ X &\in \left\{E_z^{(p)}, H_z^{(p)}\right\}, \end{aligned} \tag{30}$$

where $\operatorname{sinc}(x) = \sin(x)/x$, and we define the function $\operatorname{Iinc}(x) = 2I_1(x)/x$. The fact that the factor corresponding to the finite bunch radius Δ_r is independent of k_z is nontrivial. A detailed derivation of the bunch factor in Eq. (30) is presented in Appendix F. The secondary fields induced by the bunch may subsequently be retrieved by substituting the modified

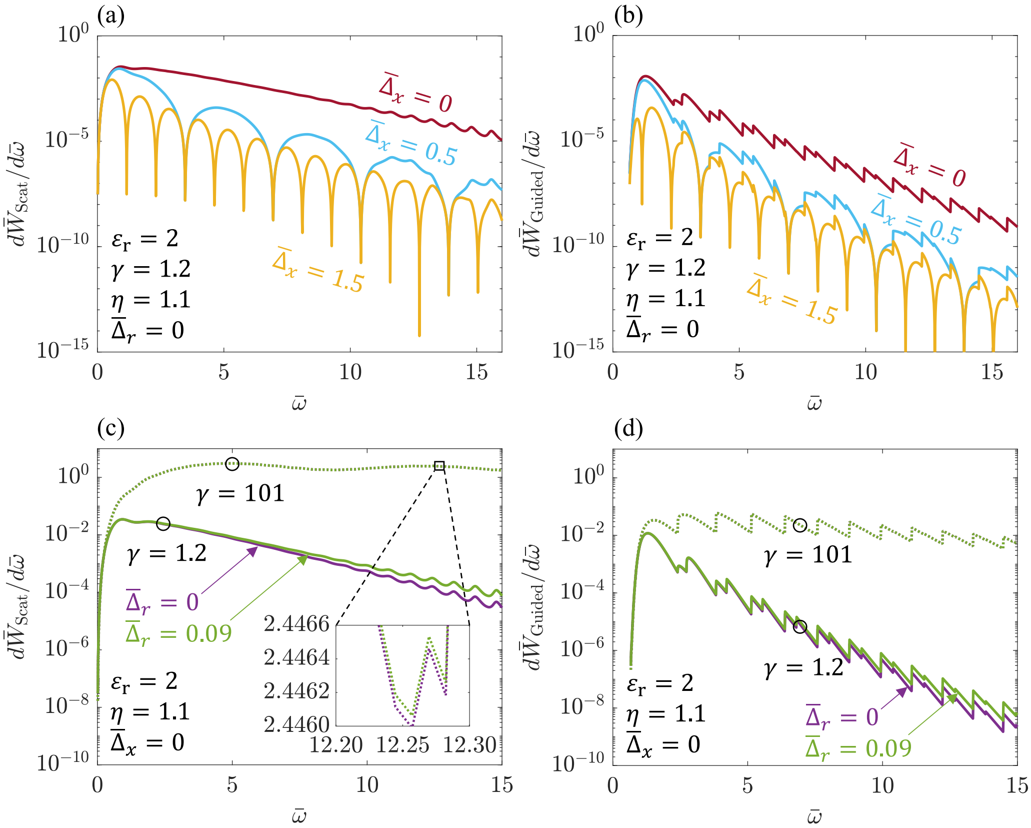

FIG. 7. The effect of a finite-size bunch on the radiation spectrum. The spectra of the scattered and guided radiation are plotted for multiple normalized bunch size parameters ($\bar{\Delta} = \Delta/R$). (a) Scattered spectrum for multiple bunch widths $\bar{\Delta}_x$ and and bunch radius $\bar{\Delta}_r = 0$. (b) Guided spectrum for multiple bunch widths $\bar{\Delta}_x$ and bunch radius $\bar{\Delta}_r = 0$. (c) Scattered spectrum for multiple kinetic energies and bunch radii $\bar{\Delta}_r$ and bunch width $\bar{\Delta}_x = 0$. The inset demonstrates the existent but negligible effect of $\bar{\Delta}_r$ on the spectrum for high energies. (d) Guided spectrum for multiple kinetic energies and bunch radii $\bar{\Delta}_r$ and bunch width $\bar{\Delta}_x = 0$.

primary field components from Eq. (30) inside the matrix equation depicted by Eq. (9).

The spectrum of the scattered and guided radiation excited by the considered bunch geometry is plotted for multiple normalized bunch widths $\bar{\Delta}_x = \Delta_x/R$ and normalized radii $\bar{\Delta}_r = \Delta_r/R$ in Fig. 7. The multiplication by a sinc function dictated by the bunch width Δ_x introduces nulls in both spectra, as apparent in Figs. 7(a) and 7(b). The null locations correspond to sinc arguments that are integer multiples of π, explicitly reading

$$\bar{\omega}_m = \pi \frac{\beta}{\bar{\Delta}_x} m, \quad m = 0, 1, 2, \ldots. \tag{31}$$

The effect of a finite bunch width remarkably resembles that of an antenna array, with the interaction of each infinitesimal bunch element with the cylinder acting as a separate antenna, consequently leading to an "array factor" in the form of a sinc function. We note that location of the first nonzero null, $\bar{\omega}_1 = \pi\beta/\bar{\Delta}_x$, allows for the estimation of the bunch velocity β or width Δ_x in a simple manner, given that the other parameter is known with high certainty. In the case of a finite bunch radius, Figs. 7(c) and 7(d) show that Δ_r leads to a minor decrease in the exponential decay rate by a factor of $2\bar{\Delta}_r/\gamma\beta$, as also predicted by the previously defined "Iinc" function in Eq. (30). The following may be attributed to the portion of the bunch that approaches the cylinder at a closer distance, leading to more significant field excitation. Although this effect appears both for low and high energies, it is rather negligible in the case of high energies due to the large value of the bunch's (normalized) momentum $\gamma\beta$.

E. Photon generation

We now examine the scattered and guided radiation emitted by the system in terms of the fundamental quantum of electromagnetic energy—the photon. Such an investigation is prompted by the potential of free electron-structure interactions in the realization of efficient single-photon sources [9]. It is warranted to define the emitted photon spectral density per electron, $\Gamma(\bar{\omega})$, such that integrating over all normalized frequencies yields the total number of emitted photons, $N_{\rm ph}$. Explicitly, $N_{\rm ph}$ is given by

$$N_{\rm ph} = \int_0^\infty d\bar{\omega}\Gamma(\bar{\omega}). \tag{32}$$

Recalling that the energy carried by a single photon with frequency ω is $\hbar\omega$ ($\hbar$ is the reduced Planck constant), the total radiated energy may be expressed as

$$W_{\rm total} = \int_0^\infty dN_{\rm ph}\hbar\omega = \frac{\hbar c}{R}\int_0^\infty d\bar{\omega}\bar{\omega}\Gamma(\bar{\omega}). \tag{33}$$

Using Eq. (33) and the definition of the normalized energy [as in Eqs. (15) and (22)] yields an expression for $\Gamma(\bar{\omega})$ in terms

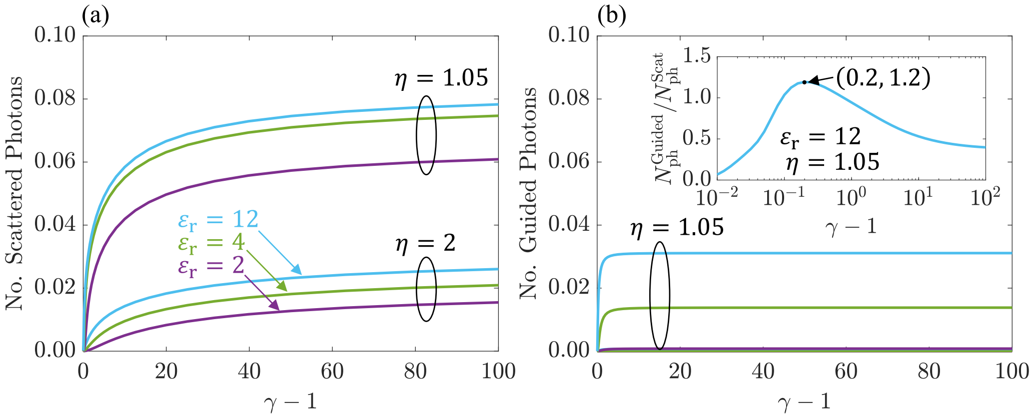

FIG. 8. Number of photons emitted per electron as scattered and guided waves. (a) Number of *scattered* photons as a function of normalized kinetic energy ($\gamma - 1$), for multiple permittivities and impact parameters. (b) Same as the previous panel, but for the *guided* photons. Here, the curves for $\eta = 2$ are too small to be seen in the given scale. The inset displays the ratio between the number of guided and scattered photons for the parameter choice $\varepsilon_r = 12$, $\eta = 1.05$, showing that the number of guided photons exceeds its scattered counterpart at the curve's maximal peak.

of the normalized spectrum:

$$\Gamma(\bar{\omega}) = \alpha \frac{1}{\bar{\omega}} \frac{d\bar{W}}{d\bar{\omega}}, \tag{34}$$

where $\alpha = e^2/4\pi\varepsilon_0\hbar c$ is the fine-structure constant, roughly equal to 1/137. Substituting the scattered or guided spectra inside Eq. (34) gives the photon distribution corresponding to each radiation type, and using Eq. (32) yields the respective emitted photon numbers.

The number of photons emitted via both scattered and guided mechanisms is plotted in Fig. 8 as a function of the particle's kinetic energy ($\gamma - 1$), for multiple values of ε_r and η. Similar to the radiated energy, the photon number also exhibits a strong dependence in both the dielectric rod's permittivity, ε_r, and the particle's impact parameter, η. For high energies ($\gamma > 10$) and large impact parameters ($\eta \gg 1$), the scattered photon number can be reasonably approximated by

$$N_{\text{ph}}^{\text{scat}} \simeq a \ln(b\gamma), \tag{35}$$

where a and b are coefficients dependent on ε_r and η. As a concrete example, the coefficients obtained for $\eta = 2$ and $\varepsilon_r = 2, 4,$ and 12 [as in Fig. 8(a)] read $a \approx 0.0048, 0.0052,$ and 0.0054 and $b \approx 0.26, 0.60,$ and 1.4016, respectively. In contrast, the number of guided photons is observed to "saturate" for high energies, with the limiting values strongly dependent on ε_r [see Fig. 8(b)].

As with the radiated energy, in most regimes the photons are emitted predominantly in the form of *scattered* waves. However, the inset of Fig. 8(b) reveals that for sufficiently large cylinder permittivity, small impact parameter, and moderately relativistic energies, the number of guided photons becomes higher than its scattered counterpart. From a practical perspective, we note that the optical setups required for measurement and manipulation of guided photons are much simpler than those for photons radiating in free space, as the latter require consideration of the observation angle and aperture size.

In terms of order of magnitude, for high energies and small impact parameters, the number of photons emitted per a single electron can reach roughly 0.08 scattered photons, and roughly 0.03 guided photons. The following photon numbers are smaller than 1, thus the proper way to interpret this result is as follows: The fields induced by a point particle of charge q are proportional to q by virtue of Maxwell's equations' linearity, therefore the radiated energy (and consequently, the emitted photon number) is proportional to q^2. This implies that a point particle of charge $q = -4e$, or equivalently, a dense charged bunch with the same charge and spatial dimensions much smaller than the minimal wavelength 200 nm, will roughly emit a single scattered (i.e., radiating in free space) photon when grazing the dielectric rod. Similarly, a dense charge distribution of charge $q = -20e$ will roughly excite 12 guided photons, which will be confined to the rod and propagate along its axis—six in each direction forming an excellent coupler to a detector.

IV. DISCUSSION

In this paper, the radiation emitted by a point particle (or finite-size bunch) moving near an infinite dielectric rod was characterized, with both the radiation due to radially scattered waves and radiation carried axially by excited cylinder eigenmodes being considered. Our comparison between the relative portions of the scattered and guided radiation out of the total emitted energy reveals multiple regimes of interest, with the relation between both radiation types in each regime neatly summarized in Table I.

If so, the only regime in which radiation in the form of guided modes exceeds the scattered radiation is, in the case of a small distance from the cylinder, low (yet relativistic) energy and large cylinder permittivity. Otherwise, scattered radiation dominates, or is at least comparable to its guided counterpart. In the case of high energies, the ratio between the guided and total energy may be roughly approximated by a decaying exponential in $\eta - 1$, divided by a power.

TABLE I. The dominant radiation mechanism (scattered or guided) in every regime of interest for the parameters $\gamma - 1$, η, and ε_r. Guided radiation is dominant in the regime of low energy, small distance from the cylinder, and large cylinder permittivity. In all other regimes, the scattered radiation dominates.

	Low energies ($0.1 < \gamma - 1 < 10$)	High energies ($\gamma - 1 \gg 1$)
Small distances ($\eta \approx 1$)	Small ε_r: Scattered dominant Large ε_r: Guided dominant	Small ε_r: Scattered dominant Large ε_r: Both mechanisms comparable
Large distances ($\eta \gg 1$)	Scattered dominant	Scattered dominant

TABLE II. Summary of the main approximations obtained in this work. Each quantity is referred to the equation inside the paper which contains its corresponding approximation.

Quantity	Approximation
Fraction of guided energy out of total, high energies ($\gamma - 1 \gg 1$)	Eq. (25)
Scattered spectrum, low energies ($0.1 < \gamma - 1 < 10$)	Eq. (26)
Scattered spectrum, high energies ($\gamma - 1 \gg 1$)	Eq. (27)
$\mathrm{EH}_{n\nu}$ mode resonance locations in guided spectrum	Eq. (29)
Number of scattered photons, high energies ($\gamma - 1 \gg 1$)	Eq. (35)

Studying the frequency spectra reveals a simple, yet powerful approximation for the *scattered* spectrum, given by a product of the cylinder's "geometric response" (in the case of high energies, the cross section of a scattered plane wave), and a decaying exponential corresponding to the particle's evanescent fields [see Eqs. (26) and (27)]. These approximations have been found to decently capture the scattered spectrum's overall trend, and in the case of high energies also its resonant behavior, as long as the particle does not graze the dielectric rod (i.e., $\eta \neq 1$). However, the low-energy approximation does not account for the geometric resonances that emerge for large rod permittivities.

As for the guided radiation, the various peaks present in the guided spectrum were found to each be uniquely mapped to a specific cylindrical eigenmode, with the significant peaks contributed by the fundamental mode HE_{11}, the decoupled TE_{01} and TM_{01} modes, and the hybrid EH_{nm} modes, which have a dominant TM component. Moreover, the locations of peaks corresponding to the EH modes, which were observed to be the most significant, have been analytically characterized in terms of these modes' cutoff frequencies. The prominence of EH modes (which are "TM-like") in the guided radiation is in sharp contrast to the scattered case, where the main contribution to the radiation was found to come from the TE component in the Poynting vector. It was additionally found that both the scattered and guided waves are mainly composed of waves rotating *clockwise*, which correspond to *negative* azimuthal harmonics (n). This azimuthal asymmetry has been intuitively associated with clockwise-rotating multipoles inside the rod, with the direction of rotation dictated by the particle's motion in the positive x direction.

Next, the effect of a finite-size cylindrical bunch on the spectrum was considered, with the bunch width Δ_x introducing periodic nulls to the spectrum and the bunch radius Δ_r slowing down its exponential decay rate. Then, the emitted scattered and guided energies were evaluated in terms of photons, showing that a coherent bunch of only a few electrons is sufficient for exciting a single photon, either radiating in free space or guided along the dielectric rod. In addition, an analytical approximation for the number of scattered photons in the case of high particle energy has been found, which scales as $\ln(b\gamma)$ for a coefficient b that depends on ε_r and η.

Perhaps the results of this paper that have the highest significance to future endeavors are the various approximations obtained for the problem's quantities of interest, analytic and quasianalytic. Their importance stems from their potential use as scaling laws for the radiation emitted in more realistic settings, such as in optical acceleration structures. The main approximations are summarized in Table II.

We stress that the above scaling laws apply only to dielectric materials that are mostly transparent below the far UV (i.e., wavelengths below 200 nm), following our assumption that the integration frequency range may be truncated at the corresponding normalized cutoff frequency, $\bar{\omega}_{\mathrm{co}} = 10\pi$ (recall Sec. III A). This limits the model's validity for certain materials, which exhibit significant dielectric response for even shorter wavelengths. An example for such material is fused quartz, whose dielectric coefficient attains resonances at wavelengths of 60, 106, and 119 nm [31]. In addition, more realistic computations must incorporate the frequency dependence of ε_r in various materials (such as the significant 288-nm resonance in silicon [31]), instead of assuming a "flat" dielectric response. Nevertheless, our results allow us to roughly assess the emitted wakefield through both scattered and guided mechanisms inside dielectric acceleration structures.

ACKNOWLEDGMENT

We acknowledge funding from the Israel Science Foundation Grant No. 646/18.

APPENDIX A: FOURIER TRANSFORM OF THE LONGITUDINAL PRIMARY FIELD COMPONENTS

In this section, we derive analytical expressions for the Fourier transform of the longitudinal (z) components of the primary electric and magnetic fields, $E_z^{(p)}$ and $H_z^{(p)}$, as depicted in Eq. (1). Assuming the point particle is located at $x = x_0, y = h,$ and $z = z_0$ at time $t = 0$ and moves at a constant velocity $\mathbf{v} = \beta c\hat{\mathbf{x}}$ (see Fig. 1), these components are given in space and time coordinates by

$$\begin{aligned}\tilde{E}_z^{(p)}(\mathbf{r},t) &= -\frac{e}{4\pi\varepsilon_0}\frac{\gamma(z-z_0)}{[\gamma^2(x-x_0-vt)^2+(y-h)^2+(z-z_0)^2]^{3/2}},\\ \tilde{H}_z^{(p)}(\mathbf{r},t) &= -\frac{e}{4\pi}\frac{\gamma v(y-h)}{[\gamma^2(x-x_0-vt)^2+(y-h)^2+(z-z_0)^2]^{3/2}},\end{aligned} \tag{A1}$$

where $\gamma = 1/\sqrt{1-\beta^2}$ is the Lorentz factor.

We perform a Fourier transform from the cylindrical ϕ and z coordinates and time coordinate t, to the coordinates n, k_z, and ω, respectively. The Fourier transform of the field components is defined according to the following convention:

$$\begin{aligned}E_z^{(p)}(\rho,n,k_z,\omega) &= \frac{1}{(2\pi)^3}\int_{-\infty}^{\infty}dte^{-j\omega t}\int_{-\infty}^{\infty}dze^{jk_z z}\int_{-\pi}^{\pi}d\phi e^{jn\phi}\tilde{E}_z^{(p)}(\mathbf{r},t),\\ H_z^{(p)}(\rho,n,k_z,\omega) &= \frac{1}{(2\pi)^3}\int_{-\infty}^{\infty}dte^{-j\omega t}\int_{-\infty}^{\infty}dze^{jk_z z}\int_{-\pi}^{\pi}d\phi e^{jn\phi}\tilde{H}_z^{(p)}(\mathbf{r},t).\end{aligned} \tag{A2}$$

We begin by evaluating $E_z^{(p)}(\rho,n,k_z,\omega)$: Using the relations $x=\rho\cos\phi$ and $y=\rho\sin\phi$ between the defined Cartesian and cylindrical coordinates, and defining

$$\xi(\phi,t) = \sqrt{\gamma^2(\rho\cos\phi - x_0 - vt)^2 + (\rho\sin\phi - h)^2}, \tag{A3}$$

we get

$$E_z^{(p)}(\rho,n,k_z,\omega) = -\frac{e}{4\pi\varepsilon_0}\frac{1}{(2\pi)^3}\gamma\int_{-\infty}^{\infty}dte^{-j\omega t}\int_{-\pi}^{\pi}d\phi e^{jn\phi}\int_{-\infty}^{\infty}dz\frac{(z-z_0)e^{jk_z z}}{[\xi^2(\phi,t)+(z-z_0)^2]^{3/2}}. \tag{A4}$$

The integral with respect to z may be simplified as follows:

$$\begin{aligned}\int_{-\infty}^{\infty}dz\frac{(z-z_0)e^{jk_z z}}{[\xi^2(\phi,t)+(z-z_0)^2]^{3/2}} &= \int_{-\infty}^{\infty}dze^{jk_z z}\frac{\partial}{\partial z}\left(-\frac{1}{\sqrt{\xi^2(\phi,t)+(z-z_0)^2}}\right) = jk_z\int_{-\infty}^{\infty}dz\frac{e^{jk_z z}}{\sqrt{\xi^2(\phi,t)+(z-z_0)^2}}\\ &= jk_z\int_{-\infty}^{\infty}dz\frac{e^{jk_z z}}{\xi(\phi,t)\sqrt{1+\left(\frac{z-z_0}{\xi(\phi,t)}\right)^2}} = jk_z\int_{-\infty}^{\infty}du\frac{e^{jk_z(z_0+\xi(\phi,t)u)}}{1+u^2} = e^{jk_z z_0}jk_z\int_{-\infty}^{\infty}du\frac{e^{jk_z\xi(\phi,t)u}}{\sqrt{1+u^2}}.\end{aligned} \tag{A5}$$

Using the following integral identity from Ref. [35],

$$K_0(x) = \int_0^{\infty}\frac{\cos(xt)}{\sqrt{t^2+1}}dt = \frac{1}{2}\int_{-\infty}^{\infty}\frac{e^{jxt}}{\sqrt{t^2+1}}dt, \quad x>0, \tag{A6}$$

we get

$$\int_{-\infty}^{\infty}dz\frac{(z-z_0)e^{jk_z z}}{[\xi^2(\phi,t)+(z-z_0)^2]^{3/2}} = e^{jk_z z_0}jk_z \times 2K_0[|k_z|\xi(\phi,t)]. \tag{A7}$$

Substituting back in Equation (A4) yields

$$E_z^{(p)}(\rho,n,k_z,\omega) = -\frac{e}{4\pi\varepsilon_0}\frac{2jk_z}{(2\pi)^3}\gamma e^{jk_z z}\int_{-\pi}^{\pi}d\phi e^{jn\phi}\int_{-\infty}^{\infty}dte^{-j\omega t}K_0[|k_z\xi(\phi,t)|]. \tag{A8}$$

The argument of $K_0(\zeta)$ may be reformulated as follows:

$$|k_z|\xi(\phi,t) = |k_z|\sqrt{\gamma^2(\rho\cos\phi - x_0 - vt)^2 + (\rho\sin\phi - h)^2} = \sqrt{(\tau-\tau_0)^2+\Delta\tau^2}, \tag{A9}$$

where we define

$$\tau = |k_z|\gamma(x_0+vt), \quad \tau_0 = |k_z|\gamma\rho\cos\phi, \quad \Delta\tau = |k_z|\gamma(\rho\sin\phi - h). \tag{A10}$$

Thus, the integral with respect to t may be simplified as follows:

$$\begin{aligned}\int_{-\infty}^{\infty}dte^{-j\omega t}K_0[|k_z|\xi(\phi,t)] &= \int_{-\infty}^{\infty}\frac{d\tau}{|k_z|\gamma v}\exp\left[-j\frac{\omega}{v}\left(\frac{\tau}{\gamma|k_z|}-x_0\right)\right]K_0[\sqrt{(\tau-\tau_0)^2+\Delta\tau^2}]\\ &= \exp\left(j\frac{\omega}{v}x_0\right)\int_{-\infty}^{\infty}\frac{d\tilde{\tau}}{|k_z|\gamma v}\exp\left(-j\frac{\omega}{\gamma v|k_z|}(\tilde{\tau}+\tau_0)\right)K_0(\sqrt{\tilde{\tau}^2+\Delta\tau^2})\\ &= \frac{1}{|k_z|\gamma v}\exp\left(j\frac{\omega}{v}x_0\right)\exp\left(-j\frac{\omega}{v}\rho\cos\phi\right)\int_{-\infty}^{\infty}d\tilde{\tau}\exp\left(-j\frac{\omega}{\gamma v|k_z|}\tilde{\tau}\right)K_0(\sqrt{\tilde{\tau}^2+\Delta\tau^2}).\end{aligned} \tag{A11}$$

Invoking the following integral identity [36],

$$\int_0^\infty K_0(\alpha\sqrt{x^2+\beta^2})\cos(\gamma x)dx = \frac{1}{2}\int_{-\infty}^{\infty} K_0(\alpha\sqrt{x^2+\beta^2})e^{-j\gamma x}dx = \frac{\pi}{2}\frac{e^{-\beta\sqrt{\alpha^2+\gamma^2}}}{\sqrt{\alpha^2+\gamma^2}}, \quad \mathrm{Re}\{\alpha\}>0, \quad \mathrm{Re}\{\beta\}>0, \tag{A12}$$

yields (assuming $\rho < h$)

$$\begin{aligned}\int_{-\infty}^{\infty} dt e^{-j\omega t}K_0[|k_z|\xi(\phi,t)] &= \frac{\pi}{|k_z|\gamma v}\exp\left(j\frac{\omega}{v}x_0\right)\exp\left(-j\frac{\omega}{v}\rho\cos\phi\right)\frac{\exp[-|\Delta\tau|\sqrt{1+(\omega/\gamma v|k_z|)^2}]}{\sqrt{1+(\omega/\gamma v|k_z|)^2}}\\ &= \frac{\pi}{\gamma v}\exp\left(j\frac{\omega}{v}x_0\right)\exp\left(-j\frac{\omega}{v}\rho\cos\phi\right)\frac{\exp\left[-\sqrt{k_z^2+(\omega/\gamma v)^2}(h-\rho\sin\phi)\right]}{\sqrt{k_z^2+(\omega/\gamma v)^2}}.\end{aligned} \tag{A13}$$

Substituting back in Eq. (A4), we get

$$\begin{aligned}E_z^{(p)}(\rho,n,k_z,\omega) = &-\frac{e}{4\pi\varepsilon_0}\frac{jk_z}{(2\pi)^2}\frac{1}{v\sqrt{k_z^2+(\omega/\gamma v)^2}}\exp\left[j\frac{\omega}{v}x_0-\sqrt{k_z^2+\left(\frac{\omega}{\gamma v}\right)^2}h+jk_zz_0\right]\\ &\times\int_{-\pi}^{\pi}d\phi e^{jn\phi}\exp\left(-j\frac{\omega}{v}\rho\cos\phi\right)\exp\left[\sqrt{k_z^2+\left(\frac{\omega}{\gamma v}\right)^2}\rho\sin\phi\right].\end{aligned} \tag{A14}$$

We employ the Jacobi-Anger expansion,

$$e^{-ja\cos\phi} = \sum_{\nu=-\infty}^{\infty}J_\nu(a)e^{j\nu(\phi-\frac{\pi}{2})}, \qquad e^{a\sin\phi} = \sum_{\nu=-\infty}^{\infty}I_\nu(a)e^{j\nu(\phi-\frac{\pi}{2})}, \tag{A15}$$

in order to simplify the integral with respect to ϕ:

$$\begin{aligned}&\int_{-\pi}^{\pi}d\phi e^{jn\phi}\exp\left(-j\frac{\omega}{v}\rho\cos\phi\right)\exp\left[\sqrt{k_z^2+\left(\frac{\omega}{\gamma v}\right)^2}\rho\sin\phi\right]\\ &= \sum_{\mu=-\infty}^{\infty}\sum_{\nu=-\infty}^{\infty}J_\mu\left(\frac{\omega}{v}\rho\right)I_\nu\left[\sqrt{k_z^2+\left(\frac{\omega}{\gamma v}\right)^2}\right]e^{-j\frac{\pi}{2}(\mu+\nu)}\int_{-\pi}^{\pi}d\phi e^{j(n+\mu+\nu)\phi}.\end{aligned} \tag{A16}$$

Orthogonality of the harmonics $\{e^{jmx}\}_{m=0}^{\infty}$ over the interval $[\pi,\pi]$ implies

$$\int_{-\pi}^{\pi}d\phi e^{j(n+\mu+\nu)\phi} = 2\pi\delta_{n+\mu+\nu}, \tag{A17}$$

where δ is Kronecker's delta function. Therefore,

$$\int_{-\pi}^{\pi}d\phi e^{jn\phi}\exp\left(-j\frac{\omega}{v}\rho\cos\phi\right)\exp\left[\sqrt{k_z^2+\left(\frac{\omega}{\gamma v}\right)^2}\rho\sin\phi\right] = 2\pi e^{j\frac{\pi}{2}n}\sum_{\mu=-\infty}^{\infty}J_\mu\left(\frac{\omega}{v}\rho\right)I_{-n-\mu}\left[\sqrt{k_z^2+\left(\frac{\omega}{\gamma v}\right)^2}\rho\right]. \tag{A18}$$

We now utilize Graf's addition theorem [37],

$$\sum_{m=-\infty}^{\infty}J_{\nu+m}(x)J_m(y)e^{jm\psi} = \left(\frac{x-ye^{-j\psi}}{x-ye^{j\psi}}\right)^{\nu/2}J_\nu(\sqrt{x^2+y^2-2xy\cos\psi}), \tag{A19}$$

and further simplify Eq. (A18):

$$\begin{aligned}&\int_{-\pi}^{\pi}d\phi e^{jn\phi}\exp\left(-j\frac{\omega}{v}\rho\cos\phi\right)\exp\left[\sqrt{k_z^2+\left(\frac{\omega}{\gamma v}\right)^2}\rho\sin\phi\right]\\ &= 2\pi e^{j\frac{\pi}{2}n}\sum_{\mu-\infty}^{\infty}J_\mu\left(\frac{\omega}{v}\rho\right)I_{n+\mu}\left[\sqrt{k_z^2+\left(\frac{\omega}{\gamma v}\right)^2}\rho\right] = 2\pi\sum_{\mu=-\infty}^{\infty}J_{n+\mu}\left[j\sqrt{k_z^2+\left(\frac{\omega}{\gamma v}\right)^2}\rho\right]J_\mu\left(\frac{\omega}{v}\rho\right)e^{-j\frac{\pi}{2}\mu}\\ &= 2\pi\left(\frac{\sqrt{k_z^2+(\omega/\gamma v)^2}-\omega/v}{\sqrt{k_z^2+(\omega/\gamma v)^2}+\omega/v}\right)^{n/2}J_n\left[\sqrt{\left(\frac{\omega}{c}\right)^2-k_z^2\rho}\right].\end{aligned} \tag{A20}$$

Substituting back in Eq. (A14), we get the following analytical expression for the Fourier transform of the longitudinal primary electric field:

$$E_z^{(p)}(\rho, n, k_z, \omega) = -\frac{e}{4\pi\varepsilon_0}\frac{jk_z}{2\pi}\frac{1}{v\sqrt{k_z^2+(\omega/\gamma v)^2}}\exp\left[j\frac{\omega}{v}x_0 - \sqrt{k_z^2+\left(\frac{\omega}{\gamma v}\right)^2}h + jk_z z_0\right]$$
$$\times\left(\frac{\sqrt{k_z^2+(\omega/\gamma v)^2}-\omega/v}{\sqrt{k_z^2+(\omega/\gamma v)^2}+\omega/v}\right)^{n/2} J_n\left[\sqrt{\left(\frac{\omega}{c}\right)^2 - k_z^2}\rho\right]. \tag{A21}$$

The Fourier transform of the longitudinal magnetic field, $H_z^{(p)}(\rho, n, k_z, \omega)$, is evaluated in a similar manner:

$$\begin{aligned} H_z^{(p)}(\rho, n, k_z, \omega) &= -\frac{e}{4\pi}\frac{1}{(2\pi)^3}\gamma v\int_{-\infty}^{\infty}dte^{-j\omega t}\int_{-\pi}^{\pi}d\phi e^{jn\phi}\int_{-\infty}^{\infty}dze^{jk_z z}\frac{(\rho\sin\phi - h)}{[\xi^2(\phi,t)+(z-z_0)^2]^{3/2}} \\ &= -\frac{e}{4\pi}\frac{1}{(2\pi)^3}\gamma v\int_{-\infty}^{\infty}dte^{-j\omega t}\int_{-\pi}^{\pi}d\phi e^{jn\phi}\int_{-\infty}^{\infty}dze^{jk_z z}\frac{\partial}{\partial h}\left(\frac{1}{\sqrt{\xi^2(\phi,t)+(z-z_0)^2}}\right) \\ &= \frac{\partial}{\partial h}\left(-\frac{e}{4\pi}\frac{1}{(2\pi)^3}\gamma v\int_{-\infty}^{\infty}dte^{-j\omega t}\int_{-\pi}^{\pi}d\phi e^{jn\phi}\int_{-\infty}^{\infty}dze^{jk_z z}\frac{\partial}{\partial h}\frac{1}{\sqrt{\xi^2(\phi,t)+(z-z_0)^2}}\right). \end{aligned} \tag{A22}$$

From Eq. (A5) we observe that

$$H_z^{(p)}(\rho, n, k_z, \omega) = \frac{1}{\varepsilon_0}\frac{1}{jk_z}v\frac{\partial}{\partial h}E_z^{(p)}(\rho, n, k_z, \omega) = -\frac{1}{\varepsilon_0}\frac{1}{jk_z}v\sqrt{k_z^2+\left(\frac{\omega}{\gamma v}\right)^2}E_z^{(p)}(\rho, n, k_z, \omega), \tag{A23}$$

leading to the following analytical expression for $H_z^{(p)}(\rho, n, k_z, \omega)$:

$$H_z^{(p)}(\rho, n, k_z, \omega) = \frac{e}{4\pi}\frac{1}{2\pi}\exp\left[j\frac{\omega}{v}x_0 - \sqrt{k_z^2+\left(\frac{\omega}{\gamma v}\right)^2}h + jk_z z_0\right]\left(\frac{\sqrt{k_z^2+(\omega/\gamma v)^2}-\omega/v}{\sqrt{k_z^2+(\omega/\gamma v)^2}+\omega/v}\right)^{n/2}J_n\left[\sqrt{\left(\frac{\omega}{c}\right)^2-k_z^2}\rho\right]. \tag{A24}$$

The expressions in Eqs. (A21) and (A24) are then used to retrieve the coefficients $A_n, \ldots, D_n$ of the secondary field, as described in the main text.

It is insightful to define the "primary field impedance," $Z(n, k_z, \omega)$, as the ratio between $E_z^{(p)}$ and $H_z^{(p)}$, explicitly reading

$$Z(n, k_z, \omega) \triangleq \frac{E_z^{(p)}(\rho, n, k_z, \omega)}{H_z^{(p)}(\rho, n, k_z, \omega)} = -\frac{1}{\varepsilon_0}\frac{jk_z}{v\sqrt{k_z^2+(\omega/\gamma v)^2}} = -j\eta_0\frac{1}{\beta}\frac{k_z}{\sqrt{k_z^2+(\omega/\gamma v)^2}}, \tag{A25}$$

where η_0 is the free-space wave impedance. In the ultrarelativistic limit ($\gamma \to \infty$), we have

$$Z(n, k_z, \omega) \xrightarrow{\gamma\to\infty} -j\eta_0\frac{k_z}{|k_z|}, \tag{A26}$$

that is, the ratio between the longitudinal electric- and magnetic-field components approaches that of a plane wave (in absolute value).

APPENDIX B: DERIVATION OF THE SCATTERED ENERGY

In this section, we derive the expression presented in Eq. (15) for the energy radiated by the radially scattered waves. The radially emitted energy is determined by integrating the radial (ρ) component of the secondary fields' Poynting vector over a cylindrical surface of radius ρ with the same axis as the dielectric rod, and taking the limit $\rho \to \infty$, explicitly reading

$$W_{\text{scat}} = \lim_{\rho\to\infty}\rho\int_{-\infty}^{\infty}dt\int_{-\infty}^{\infty}dz\int_{-\pi}^{\pi}d\phi\left(\tilde{E}_\phi^{(\text{sec})}\tilde{H}_z^{(\text{sec})} - \tilde{E}_z^{(\text{sec})}\tilde{H}_\phi^{(\text{sec})}\right). \tag{B1}$$

Invoking Parseval's identity yields a summation over the secondary field components in Fourier space:

$$W_{\text{scat}} = (2\pi)^3\lim_{\rho\to\infty}\rho\int_{-\infty}^{\infty}d\omega\int_{-\omega/c}^{\omega/c}dk_z\sum_{n=-\infty}^{\infty}\left(E_\phi^{(\text{sec})}H_z^{(\text{sec})} - E_z^{(\text{sec})}H_\phi^{(\text{sec})}\right), \tag{B2}$$

where the integration with respect to k_z is limited to the range corresponding to radially propagating waves, $|k_z| < \frac{|\omega|}{c}$, as they are the sole contributors to the scattered radiation.

In the far-field limit ($\rho \to \infty$), the $\propto \rho^{-1}$ terms of $E_\phi^{(\mathrm{sec})}$ and $H_\phi^{(\mathrm{sec})}$ may be neglected, yielding the following approximate forms:

$$E_\phi^{(\mathrm{sec})}(\rho, n, k_z, \omega) \approx -j\frac{\omega\mu_0}{k_{\mathrm{vac}}}D_n(k_z,\omega)\dot{K}_n(k_{\mathrm{vac}}\rho), \quad H_\phi^{(\mathrm{sec})}(\rho, n, k_z, \omega) \approx j\frac{\omega\varepsilon_0}{k_{\mathrm{vac}}}B_n(k_z,\omega)\dot{K}_n(k_{\mathrm{vac}}\rho). \tag{B3}$$

Substituting back in Eq. (B2), we get

$$W_{\mathrm{scat}} = (2\pi)^3 \lim_{\rho\to\infty} \rho \int_{-\infty}^{\infty} d\omega\omega \int_{-\omega/c}^{\omega/c} dk_z \sum_{n=-\infty}^{\infty} (-j)\frac{K_n^*(k_{\mathrm{vac}}\rho)\dot{K}_n(k_{\mathrm{vac}}\rho)}{k_{\mathrm{vac}}}[\varepsilon_0|B_n(k_z,\omega)|^2 + \mu_0|D_n(k_z,\omega)|^2]. \tag{B4}$$

The product $K_n^*(k_{\mathrm{vac}}\rho)\dot{K}_n(k_{\mathrm{vac}}\rho)$ is simplified using the large-argument asymptotic expansion for the modified Bessel function of the second kind [29], and noting that k_{vac} is imaginary since $|k_z| < \frac{\omega}{c}$:

$$K_n^*(k_{\mathrm{vac}}\rho)\dot{K}_n(k_{\mathrm{vac}}\rho) \approx \left\{\left(\sqrt{\frac{\pi}{2\zeta}}e^{-\zeta}\right)^*\left[-\sqrt{\frac{\pi}{2\zeta}}\left(1+\frac{1}{2\zeta}\right)e^{-\zeta}\right]\right\}_{\zeta=k_{\mathrm{vac}}\rho} \approx -\frac{\pi}{2|k_{\mathrm{vac}}\rho|}\left|e^{-k_{\mathrm{vac}}\rho}\right|^2 = -\frac{\pi}{2(-j)k_{\mathrm{vac}}\rho}, \tag{B5}$$

where once again higher-order terms in ρ^{-1} have been neglected, as they vanish in the limit $\rho \to \infty$. Substituting back in Eq. (B4) yields

$$\begin{aligned} W_{\mathrm{scat}} &= \frac{\pi}{2}(2\pi)^3 \lim_{\rho\to\infty} \rho \int_{-\infty}^{\infty} d\omega\omega \int_{-\omega/c}^{\omega/c} dk_z \sum_{n=-\infty}^{\infty} \frac{1}{-k_{\mathrm{vac}}^2\rho}[\varepsilon_0|B_n(k_z,\omega)|^2 + \mu_0|D_n(k_z,\omega)|^2] \\ &= (2\pi)^4 \int_0^{\infty} d\omega\omega \int_0^{\omega/c} dk_z \sum_{n=-\infty}^{\infty} \frac{1}{\frac{\omega^2}{c^2} - k_z^2}[\varepsilon_0|B_n(k_z,\omega)|^2 + \mu_0|D_n(k_z,\omega)|^2] \\ &= (2\pi)^4 c^2 \varepsilon \frac{1}{R} \int_0^{\infty} d\bar{\omega}\bar{\omega} \sum_{n=-\infty}^{\infty} \int_0^{\bar{\omega}} d\bar{k}_z \frac{1}{\bar{\omega}^2 - \bar{k}_z^2}[\varepsilon_0|B_n(\bar{k}_z,\bar{\omega})|^2 + \mu_0|D_n(\bar{k}_z,\bar{\omega})|^2], \end{aligned} \tag{B6}$$

where $\bar{\omega} = \frac{\omega R}{c}$ and $\bar{k}_z = k_z R$ are the normalized quantities introduced in the main text.

We introduce the following normalization for the secondary field coefficients B_n and D_n:

$$\hat{B}_n = B_n\left(\frac{e}{4\pi}\eta_0\right)^{-1}, \quad \hat{D}_n = D_n\left(\frac{e}{4\pi}\right)^{-1}. \tag{B7}$$

Substituting back, we get

$$W_{\mathrm{scat}} = \frac{e^2}{4\pi\varepsilon_0 R}\frac{1}{2}(2\pi)^3 \int_0^{\infty} d\bar{\omega}\bar{\omega} \sum_{n=-\infty}^{\infty} \int_0^{\bar{\omega}} d\bar{k}_z \frac{1}{\bar{\omega}^2 - \bar{k}_z^2}[|\hat{B}_n(\bar{k}_z,\bar{\omega})|^2 + |\hat{D}_n(\bar{k}_z,\bar{\omega})|^2]. \tag{B8}$$

Therefore, the normalized scattered energy is given by

$$\bar{W}_{\mathrm{scat}} \triangleq \frac{W_{\mathrm{scat}}}{e^2/4\pi\varepsilon_0 R} = \frac{1}{2}(2\pi)^3 \int_0^{\infty} d\bar{\omega}\bar{\omega} \sum_{n=-\infty}^{\infty} \int_0^{\bar{\omega}} d\bar{k}_z \frac{1}{\bar{\omega}^2 - \bar{k}_z^2}[|\hat{B}_n(\bar{k}_z,\bar{\omega})|^2 + |\hat{D}_n(\bar{k}_z,\bar{\omega})|^2]. \tag{B9}$$

APPENDIX C: DERIVATION OF THE GUIDED ENERGY

In this section, we derive the expression presented in Eq. (22) for the energy radiated by the cylinder's guided modes in the axial direction. The following is determined by integrating the longitudinal (z) component of the secondary fields' Poynting vector over two circular bases with infinite radii and perpendicular to the z axis, located at offsets $\pm z$ from the origin, and taking the limit $z \to \infty$, explicitly reading

$$W_{\mathrm{guided}} = \lim_{\rho\to\infty} 2 \int_{-\infty}^{\infty} dt \int_0^{\infty} d\rho\rho \int_{-\pi}^{\pi} d\phi\left(\tilde{E}_\rho^{(\mathrm{sec})}\tilde{H}_\phi^{(\mathrm{sec})} - \tilde{E}_\phi^{(\mathrm{sec})}\tilde{H}_\rho^{(\mathrm{sec})}\right), \tag{C1}$$

with integration being performed over a single base and the result subsequently multiplied by a factor of 2 due to left-right symmetry with respect to the z axis. Fourier expanding each component yields

$$\begin{aligned}
&\int_{-\infty}^{\infty} dt \int_0^{\infty} d\rho\rho \int_{-\pi}^{\pi} d\phi\big(\tilde{E}_\rho^{(\mathrm{sec})}\tilde{H}_\phi^{(\mathrm{sec})} - \tilde{E}_\phi^{(\mathrm{sec})}\tilde{H}_\rho^{(\mathrm{sec})}\big)\\
&= \int_{-\infty}^{\infty} dt \int_0^{\infty} d\rho\rho \int_{-\pi}^{\pi} d\phi \left(\begin{array}{l}
\displaystyle\sum_{n=-\infty}^{\infty}\int_{-\infty}^{\infty} d\omega \int_{-\infty}^{\infty} dk_z E_\rho^{(\mathrm{sec})}(\rho, n, k_z, \omega)e^{j(\omega t - n\phi - k_z z)}\\
\displaystyle\times\sum_{n'=-\infty}^{\infty}\int_{-\infty}^{\infty} d\omega' \int_{-\infty}^{\infty} dk_z' H_\phi^{(\mathrm{sec})}(\rho, n', k_z', \omega')e^{j(\omega' t - n'\phi - k_z' z)}\\
\displaystyle-\sum_{n=-\infty}^{\infty}\int_{-\infty}^{\infty} d\omega \int_{-\infty}^{\infty} dk_z E_\phi^{(\mathrm{sec})}(\rho, n, k_z, \omega)e^{j(\omega t - n\phi - k_z z)}\\
\displaystyle\times\sum_{n'=-\infty}^{\infty}\int_{-\infty}^{\infty} d\omega' \int_{-\infty}^{\infty} dk_z' H_\rho^{(\mathrm{sec})}(\rho, n', k_z', \omega')e^{j(\omega' t - n'\phi - k_z' z)}
\end{array}\right)\\
&= \int_0^{\infty} d\rho\rho \sum_{n=-\infty}^{\infty}\sum_{n'=-\infty}^{\infty}\int_{-\infty}^{\infty} d\omega \int_{-\infty}^{\infty} d\omega' \int_{-\infty}^{\infty} dk_z \int_{-\infty}^{\infty} dk_z'\big[E_\rho^{(\mathrm{sec})}(\rho, n, k_z, \omega)H_\phi^{(\mathrm{sec})}(\rho, n, k_z, \omega)\\
&\quad - E_\phi^{(\mathrm{sec})}(\rho, n, k_z, \omega)H_\rho^{(\mathrm{sec})}(\rho, n, k_z, \omega)\big]\int_{-\infty}^{\infty} dt e^{j(\omega+\omega')t}\int_{-\pi}^{\pi} d\phi e^{-j(n+n')\phi}e^{-j(k_z+k_z')z},
\end{aligned} \tag{C2}$$

with orthogonality of the Fourier modes simplifying the cumbersome iterated integration as follows:

$$\begin{aligned}
&\int_{-\infty}^{\infty} dt \int_0^{\infty} d\rho\rho \int_{-\pi}^{\pi} d\phi\big(\tilde{E}_\rho^{(\mathrm{sec})}\tilde{H}_\phi^{(\mathrm{sec})} - \tilde{E}_\phi^{(\mathrm{sec})}\tilde{H}_\rho^{(\mathrm{sec})}\big)\\
&= (2\pi)^2\int_0^{\infty} d\rho\rho \sum_{n=-\infty}^{\infty}\int_{-\infty}^{\infty} d\omega \int_{-\infty}^{\infty} dk_z \int_{-\infty}^{\infty} dk_z'\big[E_\rho^{(\mathrm{sec})}(\rho, n, k_z, \omega)H_\phi^{(\mathrm{sec})}(\rho, -n, k_z', -\omega) - E_\phi^{(\mathrm{sec})}(\rho, n, k_z, \omega)\\
&\quad \times H_\rho^{(\mathrm{sec})}(\rho, -n, k_z', -\omega)\big]e^{-j(k_z+k_z')z}.
\end{aligned} \tag{C3}$$

Since the fields in space and time coordinates are real valued (as physical quantities), their Fourier transforms satisfy

$$N^*(\rho, n, k_z, \omega) = N(\rho, -n, -k_z, -\omega), \quad N \in \big\{E_\rho^{(\mathrm{sec})}, E_\phi^{(\mathrm{sec})}, H_\rho^{(\mathrm{sec})}, H_\phi^{(\mathrm{sec})}\big\} \tag{C4}$$

and

$$\int_{-\infty}^{\infty} d\omega \sum_{n=-\infty}^{\infty}\int_{-\infty}^{\infty} dk_z N(\rho, n, k_z, \omega)e^{j(\omega t - n\phi - k_z z)} = 2\int_0^{\infty} d\omega \sum_{n=-\infty}^{\infty}\int_{-\infty}^{\infty} dk_z \mathrm{Re}\{N(\rho, n, k_z, \omega)e^{j(\omega t - n\phi - k_z z)}\}. \tag{C5}$$

Therefore, Eq. (C2) may be rephrased as follows:

$$\int_{-\infty}^{\infty} dt \int_0^{\infty} d\rho\rho \int_{-\pi}^{\pi} d\phi\big(\tilde{E}_\rho^{(\mathrm{sec})}\tilde{H}_\phi^{(\mathrm{sec})} - \tilde{E}_\phi^{(\mathrm{sec})}\tilde{H}_\rho^{(\mathrm{sec})}\big) = 2(2\pi)^2\int_0^{\infty} d\rho\rho \int_0^{\infty} d\omega \sum_{n=-\infty}^{\infty}\mathrm{Re}\left\{\begin{array}{l}
\displaystyle\int_{-\infty}^{\infty} dk_z e^{-jk_z z}E_\rho^{(\mathrm{sec})}(\rho, n, k_z, \omega)\\
\displaystyle\times\int_{-\infty}^{\infty} dq_z e^{jq_z z}H_\phi^{*(\mathrm{sec})}(\rho, n, q_z, \omega)\\
\displaystyle-\int_{-\infty}^{\infty} dk_z e^{-jk_z z}E_\phi^{(\mathrm{sec})}(\rho, n, k_z, \omega)\\
\displaystyle\times\int_{-\infty}^{\infty} dq_z e^{jq_z z}H_\rho^{*(\mathrm{sec})}(\rho, n, q_z, \omega)
\end{array}\right\}. \tag{C6}$$

The integration of the secondary field components with respect to k_z is obstructed for every value of n and ω by the presence of poles, $\{k_{n,s}(\omega)\}_{s=1}^{\infty}$, along the real axis. These poles are the zeros of the determinant $\Delta_n(k_z, \omega)$ of the coefficient matrix [see Eq. (13)], and correspond to the cylinder's eigenmodes. It is also important to note that $\Delta_n(k_z, \omega)$ is purely real in the range $\omega^2/c^2 < k_z^2 < \varepsilon_r\omega^2/c^2$, and is an even function of n, k_z, and ω.

In this scenario, it is convenient to define the field components multiplied by the determinant, namely,

$$N(\rho,n,k_z,\omega)=\frac{\bar{N}(\rho,n,k_z,\omega)}{\Delta_n(k_z,\omega)},\quad N\in\big\{E_\rho^{(\mathrm{sec})},E_\phi^{(\mathrm{sec})},H_\rho^{(\mathrm{sec})},H_\phi^{(\mathrm{sec})}\big\}. \tag{C7}$$

The advantage of such a representation is that $\bar{N}(\rho,n,k_z,\omega)$ is nonsingular, with all singularities encoded inside the determinant.

Next, we Taylor expand the determinant near its poles, since the main contribution to $1/\Delta_n$ comes from their vicinity. Explicitly,

$$\frac{1}{\Delta_n(k_z,\omega)}\approx\sum_{s=1}^{\infty}\frac{1}{\underbrace{\Delta_n(k_{n,s}(\omega),\omega)}_{0}+\big[\frac{\partial}{\partial k_z^2}\Delta_n(k_z,\omega)\big]_{k_z^2=k_{n,s}^2}\big(k_z^2-k_{n,s}^2\big)}=\sum_{s=1}^{\infty}\frac{2k_{n,s}}{\dot{\Delta}_{n,s}}\frac{1}{k_z^2-k_{n,s}^2}, \tag{C8}$$

where $\dot{\Delta}_{n,s}=\frac{\partial\Delta_n}{\partial k_z}(k_{n,s},\omega)$, and the ω argument of $k_{n,s}(\omega)$ is omitted for clarity. Now, the inverse transforms of the field components with respect to k_z may be evaluated. We begin with the integral containing $E_\rho^{(\mathrm{sec})}$:

$$\int_{-\infty}^{\infty}dk_z e^{-jk_z z}E_\rho^{(\mathrm{sec})}(\rho,n,k_z,\omega)=\int_{-\infty}^{\infty}dk_z e^{-jk_z z}\frac{\bar{E}_\rho^{(\mathrm{sec})}(\rho,n,k_z,\omega)}{\Delta_n(k_z,\omega)}=\sum_{s=1}^{\infty}\frac{2k_{n,s}}{\dot{\Delta}_{n,s}}\bar{E}_\rho^{(\mathrm{sec})}(\rho,n,k_{n,s},\omega)\underbrace{\int_{-\infty}^{\infty}dk_z\frac{e^{-jk_z z}}{k_z^2-k_{n,s}^2}}_{G(z;k_{n,s})}. \tag{C9}$$

The integral in $G(z;k_{n,s})$ is evaluated using residue analysis. First, simplifying a bit,

$$G(z;k_{n,s})=\int_{-\infty}^{\infty}dk_z\frac{e^{-jk_z z}}{k_z^2-k_{n,s}^2}=\frac{1}{2k_{n,s}}\bigg(\int_{-\infty}^{\infty}dk_z\frac{e^{-jk_z z}}{k_z-k_{n,s}}-\int_{-\infty}^{\infty}dk_z\frac{e^{-jk_z z}}{k_z+k_{n,s}}\bigg). \tag{C10}$$

The integrands in the above integrals have two poles on the real axis, located at $k_z=\pm k_{n,s}$. Assuming without loss of generality that $z>0$, the poles should be shifted away from the real line by introducing a negative imaginary part, in order of the integral to be well defined, Explicitly, we have

$$\pm k_{n,s}\to\pm k_{n,s}-j\delta,\quad \delta>0. \tag{C11}$$

The choice of a negative imaginary part corresponds to a lossy medium inside the cylinder, which is necessary for the uniqueness theorem to hold.

After the poles have been shifted, the real axis is closed into a semicircular integration contour in the complex plane, which contains the shifted poles (that is, closing the lower half plane). Then, Cauchy's residue theorem is invoked, and the limit $\delta\to 0$ is taken. Explicitly, the evaluation of $G(z;k_{n,s})$ proceeds as follows:

$$\begin{aligned}G(z;k_{n,s})&=\lim_{\delta\to0^+}\frac{1}{2k_{n,s}}\bigg(\int_{-\infty}^{\infty}dk_z\frac{e^{-jk_z z}}{k_z-k_{n,s}+j\delta}-\int_{-\infty}^{\infty}dk_z\frac{e^{-jk_z z}}{k_z+k_{n,s}+j\delta}\bigg)\\&=\lim_{\delta\to0^+}\frac{1}{2k_{n,s}}\bigg[-2\pi j\mathrm{Res}\bigg(\frac{e^{-jk_z z}}{k_z-k_{n,s}+j\delta};k_{n,s}-j\delta\bigg)+2\pi j\mathrm{Res}\bigg(\frac{e^{-jk_z z}}{k_z+k_{n,s}+j\delta};-k_{n,s}-j\delta\bigg)\bigg]\\&=\lim_{\delta\to0^+}\frac{1}{2k_{n,s}}(-2\pi j)(e^{-j(k_{n,s}-j\delta)z}-e^{-j(-k_{n,s}-j\delta)z})=\lim_{\delta\to0^+}\frac{2\pi}{k_{n,s}}e^{-\delta z}\sin(k_{n,s}z)=-\frac{2\pi}{k_{n,s}}\sin(k_{n,s}z),\end{aligned} \tag{C12}$$

with a negative sign added to the residue since the integration path is oriented clockwise. Substituting back in Eq. (C9), we get

$$\int_{-\infty}^{\infty}dk_z e^{-jk_z z}E_\rho^{(\mathrm{sec})}(\rho,n,k_z,\omega)=-\sum_{s=1}^{\infty}\frac{4\pi}{\dot{\Delta}_{n,s}}\bar{E}_\rho^{(\mathrm{sec})}(\rho,n,k_{n,s},\omega)\sin(k_{n,s}z). \tag{C13}$$

Next, we evaluate the integral containing $H_\phi^{*(\mathrm{sec})}$:

$$\int_{-\infty}^{\infty}dq_z e^{jq_z z}H_\phi^{*(\mathrm{sec})}(\rho,n,q_z,\omega)=\sum_{s=1}^{\infty}\frac{2k_{n,s}}{\dot{\Delta}_{n,s}}\bar{H}_\phi^{*(\mathrm{sec})}(\rho,n,k_{n,s},\omega)\underbrace{\int_{-\infty}^{\infty}dq_z\frac{e^{jq_z z}}{q_z^2-k_{n,s}^2}}_{G(-z;k_{n,s})}. \tag{C14}$$

From the observation that $G(z;k_{n,s})$ is symmetric with respect to z, it can be immediately deduced that the above integral results in an identical expression to Eq. (C13). The integrals containing $E_\phi^{(\mathrm{sec})}$ and $H_\rho^{*(\mathrm{sec})}$ are evaluated in a similar manner.

Substituting back in Eq. (C6) yields

$$W_{\mathrm{guided}}=\lim_{z\to\infty}(4\pi)^2\int_0^{\infty}d\omega\sum_{n=-\infty}^{\infty}\sum_{s,s'=1}^{\infty}\frac{(4\pi)^2}{\dot{\Delta}_{n,s}\dot{\Delta}_{n,s'}}\sin(k_{n,s}z)\sin(k_{n,s'}z)\mathrm{Re}\{\mathcal{I}_{s,s'}\}, \tag{C15}$$

where $\mathcal{I}_{s,s'}$ denotes

$$\mathcal{I}_{s,s'} = \int_0^\infty d\rho\rho\big[\bar{E}_\rho^{(\mathrm{sec})}(k_{n,s})\bar{H}_\phi^{*(\mathrm{sec})}(k_{n,s'}) - \bar{E}_\phi^{(\mathrm{sec})}(k_{n,s})\bar{H}_\rho^{*(\mathrm{sec})}(k_{n,s'})\big](\rho), \tag{C16}$$

which is essentially an inner product between the induced fields corresponding to different radial numbers s and s'.

It is known that for every value of $n, k_z,$ and ω, the various modes of the dielectric rod waveguide (with different radial numbers z) form an orthogonal set with respect to the inner product depicted in Eq. (C16) [30]. Inspecting a specific eigenvalue $k_{n,s}$, the corresponding normalized fields $\bar{E}_\rho^{(\mathrm{sec})}, \bar{E}_\phi^{(\mathrm{sec})}, \bar{H}_\rho^{(\mathrm{sec})},$ and $\bar{H}_\phi^{(\mathrm{sec})}$ are derived from coefficients $\bar{A}_n, \bar{B}_n, \bar{C}_n,$ and $\bar{D}_n$ which satisfy [according to Eq. (12)]

$$\begin{pmatrix} \bar{A}_n \\ \eta_0\bar{C}_n \end{pmatrix} = \begin{pmatrix} M_{22} & -M_{12} \\ -M_{21} & M_{11} \end{pmatrix}\begin{pmatrix} \eta_0 H_\phi^{(\mathrm{eff})} \\ E_\phi^{(\mathrm{eff})} \end{pmatrix}, \tag{C17}$$

$$\begin{pmatrix} \bar{B}_n \\ \eta_0\bar{D}_n \end{pmatrix} = \frac{1}{K_n}\left[\begin{pmatrix} \bar{A}_n \\ \eta_0\bar{C}_n \end{pmatrix} I_n - \underbrace{\Delta_n(k_{n,s}(\omega), \omega))}_{0}\begin{pmatrix} E_z^{(p)} \\ \eta_0 H_z^{(p)} \end{pmatrix}\right] = \begin{pmatrix} \bar{A}_n \\ \eta_0\bar{C}_n \end{pmatrix}\frac{I_n}{K_n}, \tag{C18}$$

with $E_\phi^{(\mathrm{eff})}$ and $\eta_0 H_\phi^{(\mathrm{eff})}$ defined in Eq. (12). The coefficients $\bar{A}_n$ and $\bar{C}_n$ are observed to satisfy

$$\begin{pmatrix} M_{11} & M_{12} \\ M_{21} & M_{22} \end{pmatrix}\begin{pmatrix} \bar{A}_n \\ \eta_0\bar{C}_n \end{pmatrix} = \underbrace{\Delta_n(k_{n,s}(\omega), \omega))}_{0}\mathbf{I}_{2\times 2}\begin{pmatrix} \eta_0 H_\phi^{(\mathrm{eff})} \\ E_\phi^{(\mathrm{eff})} \end{pmatrix} = \begin{pmatrix} 0 \\ 0 \end{pmatrix}, \tag{C19}$$

thus both $\bar{A}_n$ and $\bar{C}_n$ and $\bar{B}_n$ and $\bar{D}_n$ [as seen from Eq. (C18)] constitute solutions to the homogeneous electromagnetic problem. If so, the components $\bar{E}_\rho^{(\mathrm{sec})}, \bar{E}_\phi^{(\mathrm{sec})}, \bar{H}_\rho^{*(\mathrm{sec})},$ and $\bar{H}_\phi^{*(\mathrm{sec})}$, although induced following an inhomogeneous excitation (namely, the point charge), solve the homogeneous eigenvalue problem of the cylindrical dielectric waveguide when substituting $k_z = k_{n,s}(\omega)$. This implies that the aforementioned mode orthogonality relation applies also to the normalized secondary field components, therefore

$$\mathcal{I}_{s,s'} = 0, \quad \forall s \neq s'. \tag{C20}$$

Equation (C20) allows us to discard cross terms in the summation of s and s' in Eq. (C15), yielding

$$W_{\mathrm{guided}} = \lim_{z\to 0}(4\pi)^2\int_0^\infty d\omega\sum_{n=-\infty}^{\infty}\sum_{s=1}^{\infty}\left(\frac{4\pi}{\dot{\Delta}_{n,s}}\right)^2\sin^2(k_{n,s}z)\mathrm{Re}\left\{\int_0^\infty d\rho\rho\left(\bar{E}_\rho^{(\mathrm{sec})}\bar{H}_\phi^{*(\mathrm{sec})} - \bar{E}_\phi^{(\mathrm{sec})}\bar{H}_\rho^{*(\mathrm{sec})}\right)_{k_z=k_{n,s}}\right\}. \tag{C21}$$

In the limit $z \to \infty$, the argument of $\sin(k_{n,s}z)$ changes rapidly with $k_{n,s}$, thus $\sin^2(k_{n,s}z)$ may be approximated by its average value during a single period, that is, $\sin^2(k_{n,s}z) \approx \frac{1}{2}$.

As with the previously calculated scattered radiation, we introduce the following normalized field components:

$$\hat{E}_\nu = \bar{E}_\nu^{(\mathrm{sec})}\left(\frac{e}{4\pi}\eta_0\right)^{-1}, \quad \hat{H}_\nu = \bar{H}_\nu^{(\mathrm{sec})}\left(\frac{e}{4\pi}\right)^{-1}, \quad \nu \in \{\rho, \phi\}. \tag{C22}$$

Substituting back in Eq. (C21), along with the "average-power" approximation for $\sin^2(k_{n,s}z)$, in the asymptotic limit ($z \to \infty$) we get

$$\begin{aligned} W_{\mathrm{guided}} &= \frac{1}{2}(4\pi)^2\eta_0 e^2\int_0^\infty d\omega\sum_{n=-\infty}^{\infty}\sum_{s=1}^{\infty}\frac{1}{\dot{\Delta}_{n,s}^2}\mathrm{Re}\left\{\int_0^\infty d\rho\rho(\hat{E}_\rho\hat{H}_\phi^* - \hat{E}_\phi\hat{H}_\rho^*)_{k_z=k_{n,s}}\right\} \\ &= \frac{1}{2}(4\pi)^3\frac{e^2}{4\pi\varepsilon_0 R}\int_0^\infty d\bar{\omega}\sum_{n=-\infty}^{\infty}\sum_{s=1}^{\infty}\frac{1}{\dot{\Delta}_{n,s}^2}\mathrm{Re}\left\{\int_0^\infty d\bar{\rho}\bar{\rho}(\hat{E}_\rho\hat{H}_\phi^* - \hat{E}_\phi\hat{H}_\rho^*)_{\bar{k}_z=k\bar{k}_{n,s}}\right\}, \end{aligned} \tag{C23}$$

where $\bar{\rho} = \rho/R$, and now $\dot{\Delta}_{n,s}$ denotes the derivative of $\Delta_{n,s}$ with respect to $\bar{k}_z = k_z R$. Therefore, the normalized guided energy is given by

$$\bar{W}_{\mathrm{guided}} \triangleq \frac{W_{\mathrm{guided}}}{e^2/4\pi\varepsilon_0 R} = \frac{1}{2}(4\pi)^3\frac{e^2}{4\pi\varepsilon_0 R}\int_0^\infty d\bar{\omega}\sum_{n=-\infty}^{\infty}\sum_{s=1}^{\infty}\frac{1}{\dot{\Delta}_{n,s}^2}\mathrm{Re}\left\{\int_0^\infty d\bar{\rho}\bar{\rho}(\hat{E}_\rho\hat{H}_\phi^* - \hat{E}_\phi\hat{H}_\rho^*)_{\bar{k}_z=k\bar{k}_{n,s}}\right\}. \tag{C24}$$

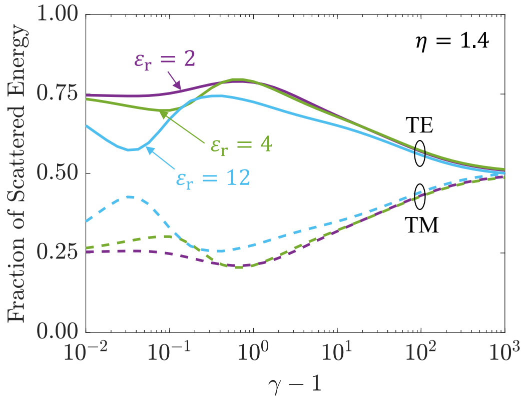

FIG. 9. Comparison between the relative portions of the TE and TM components out of the total scattered energy. The relative portions of $W_{\text{scat}}^{(\text{TE})}$ (solid curves) and $W_{\text{scat}}^{(\text{TM})}$ (dashed curves) are plotted as a function of the particle's normalized kinetic energy, $\gamma - 1$, for multiple dielectric coefficients: $\varepsilon_r = 2$ (purple), $\varepsilon_r = 4$ (green), and $\varepsilon_r = 12$ (blue). An impact parameter of $\eta = 1.4$ was used in all simulations.

APPENDIX D: COMPARISON BETWEEN THE TE AND TM COMPONENTS OF THE SCATTERED RADIATION

The expressions in Eqs. (B4) and their substitution in the expression of the scattered energy [see Eq. (B2)] show that the $\sim|B_n|^2$ term is proportional to $E_z^{(\text{sec})}H_\phi^{*(\text{sec})}$, whereas the $\sim|D_n|^2$ term is proportional to $E_\phi^{(\text{sec})}H_z^{*(\text{sec})}$. The former does not depend on the longitudinal (z) magnetic field and is thus denoted as TM. Similarly, the latter does not depend on the longitudinal electric field, and is thus denoted as TE. It is the purpose of this section to compare the TE and TM contributions to the scattered radiation.

From Eq. (B9) we can identify the normalized TE and TM contributions to the scattered energy, that is, $\bar{W}_{\text{scat}} = \bar{W}_{\text{scat}}^{(\text{TE})} + \bar{W}_{\text{scat}}^{(\text{TM})}$, where

$$\begin{aligned}\bar{W}_{\text{scat}}^{(\text{TE})} &= \frac{1}{2}(2\pi)^3\int_0^\infty d\bar{\omega}\bar{\omega}\sum_{n=-\infty}^{\infty}\int_0^{\bar{\omega}} d\bar{k}_z\frac{1}{\bar{\omega}^2-\bar{k}_z^2}|\hat{D}_n(\bar{k}_z,\bar{\omega})|^2,\\ \bar{W}_{\text{scat}}^{(\text{TM})} &= \frac{1}{2}(2\pi)^3\int_0^\infty d\bar{\omega}\bar{\omega}\sum_{n=-\infty}^{\infty}\int_0^{\bar{\omega}} d\bar{k}_z\frac{1}{\bar{\omega}^2-\bar{k}_z^2}|\hat{B}_n(\bar{k}_z,\bar{\omega})|^2.\end{aligned} \tag{D1}$$

The relative portions of $\bar{W}_{\text{scat}}^{(\text{TE})}$ and $\bar{W}_{\text{scat}}^{(\text{TM})}$ out of the total scattered energy are plotted as a function of $\gamma - 1$ in Fig. 9 for multiple values of ε_r. While the exact behavior of $\bar{W}_{\text{scat}}^{(\text{TE})}$ and $\bar{W}_{\text{scat}}^{(\text{TM})}$ is rather complicated, it can be seen that the TE contribution to the scattered energy is more significant than TM. The dominance of the TE contribution can be explained by the formation of dipole moments (or higher multipoles) inside the rod, with their orientations rotating with the change in the particle's position during its motion. These circulating multipoles generate significant azimuthal electric fields ($E_\phi^{(\text{sec})}$) and longitudinal magnetic fields ($H_z^{(\text{sec})}$), both of which are associated with the TE term. In the limit $\gamma \to \infty$, the ratio between the two terms approaches 1, in alignment with the fact that the ratio between the primary electric and magnetic (time free-space wave impedance) fields also approaches unity, as in a plane wave.

APPENDIX E: CONTRIBUTION OF AZIMUTHAL HARMONICS TO THE RADIATION

The expressions for both scattered and guided radiation include a summation over all indices $n = 0, \pm1, \pm2, \ldots$, which correspond to the family $\{e^{-jn\phi}\}_{n=-\infty}^{\infty}$ of waves rotating azimuthally around the cylinder. Given ω is positive, positive values of n represent waves rotating *counterclockwise*, whereas negative values of n represent waves rotating *clockwise*.

Taking a specific term of this sum yields the contribution of a specific azimuthal harmonic to the emitted radiation, which explicitly reads for the scattered and guided components

$$\begin{aligned}\bar{W}_{\text{scat},n} = {} & \frac{1}{2}(2\pi)^3\int_0^\infty d\bar{\omega}\bar{\omega}\int_0^{\bar{\omega}} d\bar{k}_z\frac{1}{\bar{\omega}^2-\bar{k}_z^2}\\ & \times[|\hat{B}_n(\bar{k}_z,\bar{\omega})|^2+|\hat{D}_n(\bar{k}_z,\bar{\omega})|^2],\end{aligned} \tag{E1}$$

$$\begin{aligned}\bar{W}_{\text{guided},n} = {} & \frac{1}{2}(4\pi)^3\int_0^\infty d\bar{\omega}\sum_{s=1}^{\infty}\frac{1}{\bar{\Delta}_{n,s}^2}\\ & \times\text{Re}\left\{\int_0^\infty d\bar{\rho}\bar{\rho}(\hat{E}_\rho\hat{H}_\phi^*-\hat{E}_\phi\hat{H}_\rho^*)_{\bar{k}_z=\bar{k}_{n,s}}\right\}.\end{aligned} \tag{E2}$$

The contributions of the various azimuthal harmonics to the scattered and guided energies are presented in Fig. 10 for multiple regimes of interest. For low energies ($\gamma - 1 \ll 1$) and large distances from the cylinder ($\eta \gg 1$), the dominant contribution to the energy comes in both mechanisms from the $n = -1$ harmonic, which corresponds to a clockwise-rotating wave with the symmetry of a dipole. The following may be readily explained by the formation of dipole moments inside the cylinder, with the clockwise rotation dictated by the point particle's direction of motion. However, for higher energies and smaller impact parameters, contributions due to higher harmonics become more significant, and a larger number of harmonics must be taken into account during computation. For example, for $\varepsilon_r = 4$, $\gamma - 1 = 100$, and $\eta = 1.1$, the scattered radiation roughly spans over harmonics in the range $n = -40, \ldots, 40$.

An important feature common to all regimes is the large asymmetry between positive and negative harmonics, with the energy contributed primarily by negative values of n. As mentioned above, negative harmonics correspond to waves rotating clockwise around the cylinder, and can once again be attributed to clockwise-rotating dipoles (and additional multipoles of higher order for higher energies), induced inside the cylinder by the particle's fields during its motion.

APPENDIX F: BUNCH FACTOR OF A UNIFORM, CYLINDRICAL CHARGED BUNCH

In this section, we derive the factors that multiply the primary fields' Fourier components in order to account for a uniform cylindrical bunch, as presented in Eq. (30) in the main text. We begin by considering an arbitrary bounded charge distribution Σ with charge density $\rho_e(\mathbf{r})$ at time $t = 0$ (different from the radial coordinate ρ), moving at a constant

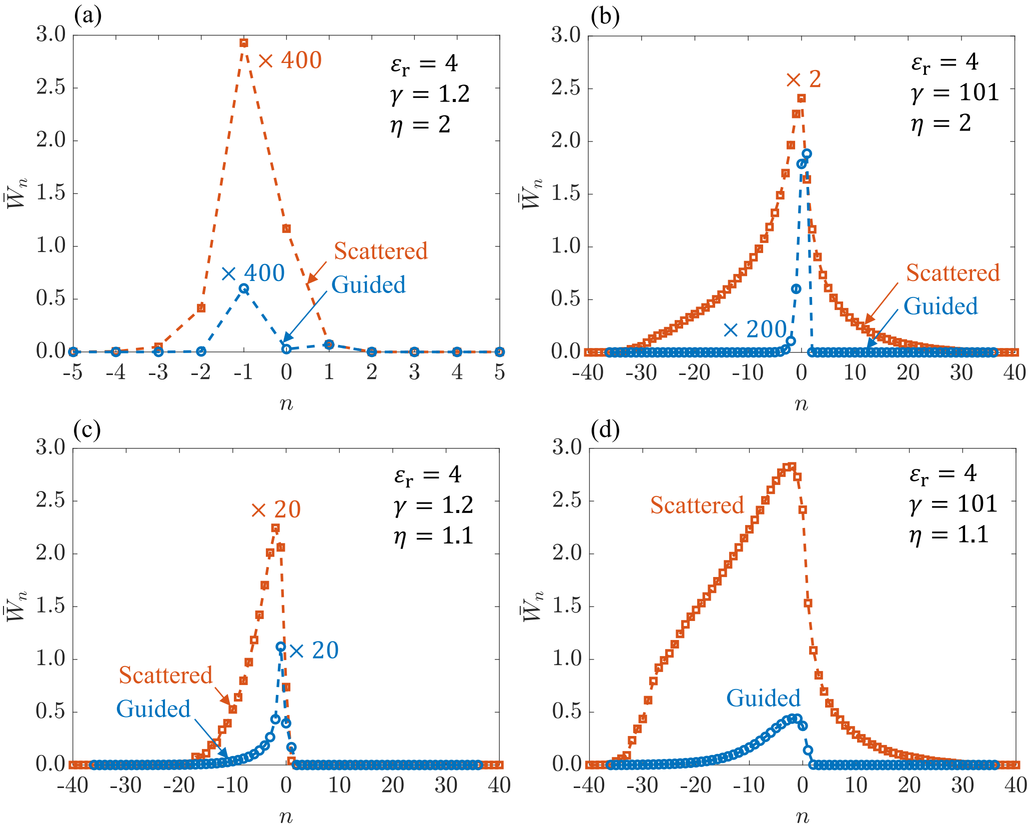

FIG. 10. Contribution of the various azimuthal harmonics to the radiated energy. The plots show the contributions to the normalized scattered and guided energy, $\bar{W}_{\text{scat}}$ and $\bar{W}_{\text{guided}}$, as a function of the harmonic index n, in the following regimes. (a) Low energy, large distance from the cylinder. (b) High energy, large distance. (c) Low energy, small distance. (d) High energy, small distance. Curves with small values are scaled by a multiplicative factor for clarity.

velocity $v = \beta c\hat{\mathbf{x}}$ similar to the point particle. By virtue of superposition, and assuming the observation point lays strictly below the bunch Σ, the Fourier transform of the longitudinal components of the corresponding primary electric field is given by [according in Eq. (A21)]

$$\begin{aligned} E_z^{(\text{bunch})}(\rho, n, k_z, \omega) &= \int_\Sigma d\mathbf{r}'\rho_{\text{e}}(\mathbf{r}')\frac{1}{4\pi\varepsilon_0}\frac{jk_z}{2\pi}\exp\left[j\frac{\omega}{v}x' - \sqrt{k_z^2 + \left(\frac{\omega}{\gamma v}\right)^2}y' + jk_z z'\right] \\ &\quad \times \left(\frac{\sqrt{k_z^2 + (\omega/\gamma v)^2} - \omega/v}{\sqrt{k_z^2 + (\omega/\gamma v)^2} + \omega/v}\right)^{n/2} J_n\left[\sqrt{\left(\frac{\omega}{c}\right)^2 - k_z^2}\,\rho\right] \\ &= E_z^{(p)}(\rho, n, k_z, \omega) \times \Lambda(n, k_z, \omega; \Sigma), \end{aligned} \tag{F1}$$

where $E_z^{(p)}(\rho, n, k_z, \omega)$ is the primary field of a point particle with charge $-e$ and impact parameter $y = h$ [as presented in Eq. (A21)], and $\Lambda(n, k_z, \omega; \Sigma)$ is a bunch factor, incorporating the bunch's geometry and charge distribution. The bunch factor explicitly reads

$$\Lambda(n, k_z, \omega; \Sigma) = \frac{1}{-e}\int_\Sigma d\mathbf{r}'\rho_{\text{e}}(x', h + y', z')\exp\left[j\frac{\omega}{v}x' - \sqrt{k_z^2 + \left(\frac{\omega}{\gamma v}\right)^2}y' + jk_z z'\right]. \tag{F2}$$

Similarly, for the primary magnetic field we have

$$H_z^{(\text{bunch})}(\rho, n, k_z, \omega) = H_z^{(p)}(\rho, n, k_z, \omega) \times \Lambda(n, k_z, \omega; \Sigma). \tag{F3}$$

In what follows, we determine $\Lambda(n, k_z, \omega; \Sigma)$ for a cylindrical bunch with uniform charge density (total charge $-e$) and an axis parallel to the x axis. As described in the main text, the cylindrical bunch is characterized by a width of $2\Delta_x$ and a base radius of Δ_r, with the bunch radius constrained to satisfy $\Delta_r < h - R$ to prevent direct contact between the bunch and the dielectric rod. The bunch's geometry may be conveniently parametrized as follows:

$$\Sigma = \left\{ (x, h + r\cos\theta, r\sin\theta) : \begin{array}{r} -\Delta_x \leqslant x \leqslant \Delta_x, \\ 0 \leqslant r \leqslant \Delta r, \\ 0 \leqslant \theta < 2\pi \end{array} \right\}. \tag{F4}$$

Substituting back in Eq. (F2), we get

$$\begin{aligned} \Lambda(n, k_z, \omega; \Delta_x, \Delta_r) &= \frac{1}{2\pi \Delta_r^2 \Delta_x} \int_{-\pi}^{\pi} d\theta' \int_0^{\Delta_r} dr' r' \int_{-\Delta_x}^{\Delta_x} \exp\left[j\frac{\omega}{v}x' - \sqrt{k_z^2 + \left(\frac{\omega}{\gamma v}\right)^2} r' \cos\theta' + jk_z r' \sin\theta' \right] \\ &= \underbrace{\frac{1}{2\Delta_x} \int_{-\Delta_x}^{\Delta_x} dx' \exp\left(j\frac{\omega}{v}x' \right)}_{\Lambda_x(n,k_z,\omega;\Delta_x)} \times \underbrace{\frac{1}{\pi \Delta_r^2} \int_0^{\Delta_r} dr' r' \int_{-\pi}^{\pi} d\theta' \exp\left[\sqrt{k_z^2 + \left(\frac{\omega}{\gamma v}\right)^2} r' \cos\theta' + jk_z r' \sin\theta' \right]}_{\Lambda_r(n,k_z,\omega;\Delta_r)}. \end{aligned} \tag{F5}$$

The factor $\Lambda_x(n, k_z, \omega; \Delta_x)$, corresponding to the bunch's finite width, is rather simple to evaluate:

$$\Lambda_x(n, k_z, \omega; \Delta_x) = \frac{1}{2\Delta_x} \int_{-\Delta_x}^{\Delta_x} dx' \exp\left(j\frac{\omega}{v}x' \right) = \frac{\exp\left(j\frac{\omega}{v}\Delta_x \right) - \exp\left(-j\frac{\omega}{v}\Delta_x \right)}{2j\frac{\omega}{v}\Delta_x} = \operatorname{sinc}\left(\frac{\omega}{v}\Delta_x \right), \tag{F6}$$

where $\operatorname{sinc}(x) \triangleq \sin x/x$. As for the factor $\Lambda_r(n, k_z, \omega; \Delta_r)$ corresponding to the bunch's finite radius, evaluation is more complicated. The integral with respect to θ' may be simplified using the following integral identity [adapted from Ref. [3] Sec. 3.338 Eq. (4)]:

$$\int_{-\pi}^{\pi} d\theta \exp(a\cos\theta + jb\sin\theta) = 2\pi I_0(\sqrt{a^2 - b^2}) \quad a, b \in \mathbb{R}, \tag{F7}$$

yielding

$$\begin{aligned} \Lambda_r(n, k_z, \omega; \Delta_r) &= \frac{1}{\pi \Delta_r^2} \int_0^{\Delta_r} dr' r' 2\pi I_0\left(\frac{\omega r'}{\gamma v} \right) \\ &= \frac{2}{\Delta_r^2} \left(\frac{\gamma v}{\omega} \right)^2 \int_0^{\frac{\omega \Delta_r}{\gamma v}} du u I_0(u) \\ &= \frac{2}{\Delta_r^2} \left(\frac{\gamma v}{\omega} \right)^2 \times \frac{\omega \Delta_r}{\gamma v} I_1\left(\frac{\omega \Delta_r}{\gamma v} \right) \\ &= 2\frac{I_1(\omega \Delta_r/\gamma v)}{\omega \Delta_r/\gamma v} \\ &= \operatorname{Iinc}\left(\frac{\omega}{\gamma v}\Delta_r \right), \end{aligned} \tag{F8}$$

where we define $\operatorname{Iinc}(x) \triangleq 2I_1(x)/x$. Putting it all together, the bunch factor corresponding to the cylindrical bunch is given by

$$\begin{aligned} &\Lambda(n, k_z, \omega; \Delta_x, \Delta_r) \\ &\quad = \Lambda_x(n, k_z, \omega; \Delta_x)\Lambda_r(n, k_z, \omega; \Delta_r) \\ &\quad = \operatorname{sinc}\left(\frac{1}{\beta}\frac{\omega}{c}\Delta_x \right) \operatorname{Iinc}\left(\frac{1}{\gamma\beta}\frac{\omega}{c}\Delta_r \right). \end{aligned} \tag{F9}$$

APPENDIX G: NAMING CONVENTIONS FOR CYLINDRICAL WAVEGUIDE MODES

It is the purpose of this section to reconcile the naming scheme used to denote the guided modes in a cylindrical, dielectric waveguide in our theoretical analysis with the convention commonly used in the literature. In our formulation, each mode corresponds to two integer indices: an azimuthal harmonic $n = 0, \pm 1, \pm 2, \ldots$, which describes the mode's rotatory behavior around the cylinder, and a radial harmonic $s = 1, 2, 3, \ldots$, which describes the mode's oscillatory behavior in the radial direction. On the other hand, it is common in the literature (e.g., textbooks on optical fibers) to categorize the modes also by the polarization: For $n = 0$ (i.e., circular symmetric waves), the modes can be decoupled into pure TE and pure TM components, labeled as TE_{0m} and TM_{0m}, where $m =, 1, 2, 3, \ldots$. The first (i.e., smallest k_z) mode for $n = 0$ is of TE polarization, and the higher-order modes have alternating polarizations. Therefore, the TE_{0m} and TM_{0m} modes correspond to odd and even values of s, respectively. For values of n larger than zero, the modes

TABLE III. Conversion between the different naming schemes for the guided modes of a cylindrical dielectric waveguide. Each row and column correspond to specific values of n and s, and the corresponding cell contains the mode's name according to the convention common in the literature.

	$n = 0$	$n = \pm 1$	$n = \pm 2$	$n = \pm 3$	$n = \pm 4$
$s = 1$	TE_{01}	HE_{11}	HE_{21}	HE_{31}	HE_{41}
$s = 2$	TM_{01}	EH_{11}	EH_{21}	EH_{31}	EH_{41}
$s = 3$	TE_{02}	HE_{12}	HE_{22}	HE_{32}	HE_{42}
$s = 4$	TM_{02}	EH_{12}	EH_{22}	EH_{32}	EH_{42}
$s = 5$	TE_{03}	HE_{13}	HE_{23}	HE_{33}	HE_{43}

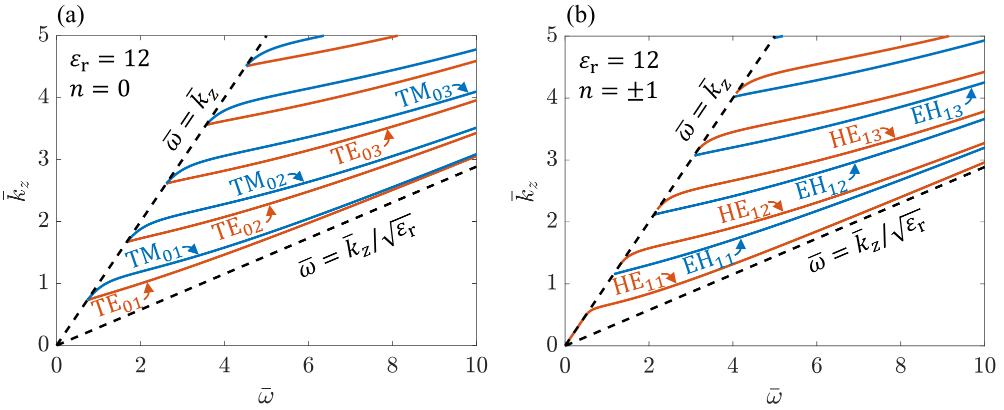

FIG. 11. Dispersion curves of the dielectric cylinder's guided modes. The dispersion curves (colored solid lines) are plotted in normalized coordinates $\bar{k}_z = k_z R$, $\bar{\omega} = \omega R/c$ for a cylinder relative permittivity of $\varepsilon_r = 12$ and the azimuthal harmonics (a) $n = 0$ and (b) $n = \pm 1$. The mode types of the first few bands are also denoted. The black dashed lines correspond to the lines $\bar{\omega} = \bar{k}_z$ and $\bar{k}_z/\sqrt{\varepsilon_r}$, with the various dispersion curves strictly lying between the two.

can no longer be separated into TE and TM components. These modes are called *hybrid modes*, and can also be divided into two types: HE$_{nm}$ modes, which have a dominant TE component (but nonvanishing TM component), and EH$_{nm}$ modes, which have a dominant TM component (but nonvanishing TE component). Similar to the case for $n = 0$, the first mode for a given value of $n > 0$ is of the HE type, with the higher-order modes alternating between EH and HE. Therefore, the HE$_{nm}$ and EH$_{nm}$ modes also correspond to odd and even values of s, respectively.

Table III demonstrates the conversion between the two naming schemes for select values of s, and Fig. 11 displays the dispersion curves (mode frequency ω as a function of its wave number k_z) for $n = 0$ and 1.

APPENDIX H: EFFECT OF A LOSSY MEDIUM ON THE SCATTERED RADIATION

This section is devoted to the inspection of the scattered spectrum in the presence of losses inside the dielectric cylinder. Losses may be easily incorporated by adding a negative imaginary part to the dielectric coefficient, corresponding to the following transformation:

$$\varepsilon_r \rightarrow \varepsilon_r - j\delta, \quad \delta \geqslant 0. \tag{H1}$$

The value of δ can be chosen to match the dielectric losses of realistic materials. Our discussion is, however, motivated mainly by numerical considerations: When evaluating the scattered energy and spectrum of values of ε_r and for $\eta \approx 1$, significant numerical noise begins to emerge. Figure 12 displays the scattered spectrum for multiple "loss magnitudes" δ for $\eta \approx 1.05$, $\gamma = 1.2$, and $\varepsilon_r = 4$, 12—a choice of parameters leading to significant numerical artifacts in the absence of losses. The following plots demonstrate that introducing losses removes numerical noise from the spectrum and retains only the "authentic" resonant peaks, with negligible effect on the spectrum's overall height. In our simulation, for $\varepsilon_r = 4$ taking $\delta = 10^{-2}$ is sufficient in order to remove numerical noise, yet for $\varepsilon_r = 12$ taking $\delta = 10^{-1}$ is required. The following are the values of δ used in the numerical computations which produce the results presented in the main text.

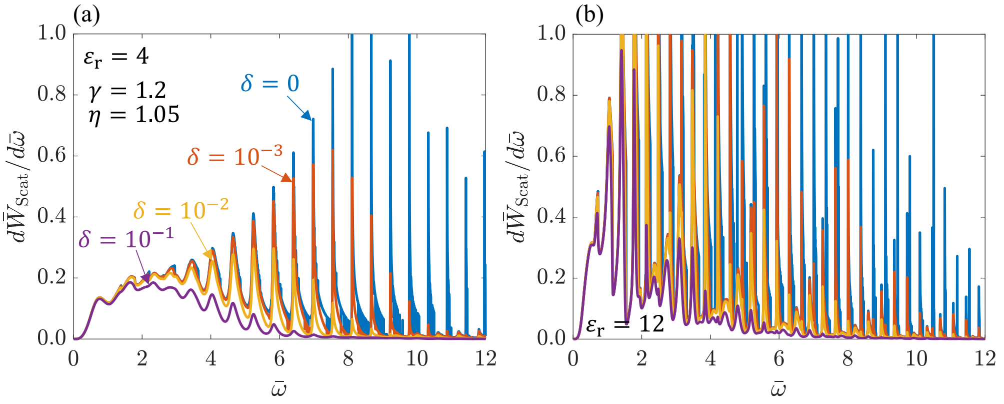

FIG. 12. Scattered spectrum in the presence of losses. The spectrum is plotted for multiple "loss magnitudes" $\delta \geqslant 0$, with the lossy dielectric coefficient given by $\varepsilon_r - j\delta$. The parameters $\gamma = 1.2$ and $\eta = 1.05$ were used in simulation, with the real part of the permittivity being (a) $\varepsilon_r = 4$ and (b) $\varepsilon_r = 12$.

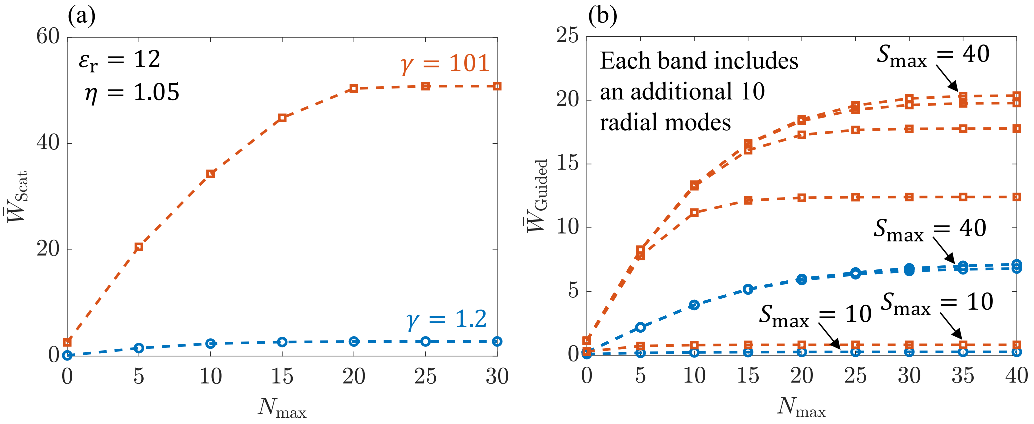

FIG. 13. Evaluated energy as a function of the truncation bounds of the harmonics. (a) Scattered energy resulting from summation of harmonics in the range $n = -N_{\mathrm{max}}, \dots, N_{\mathrm{max}}$ as a function of N_{max}, plotted for both $\gamma = 1.2$ (blue with circular markers) and $\gamma = 101$ (red with square markers). (b) Guided energy resulting from summation of azimuthal and radial harmonics in the ranges $n = -N_{\mathrm{max}}, \dots, N_{\mathrm{max}}$ and $s = 1, \dots, S_{\mathrm{max}}$, respectively, as a function of N_{max} and S_{max}, plotted for both $\gamma = 1.2$ and 101. The first band corresponds to $S_{\mathrm{max}} = 10$ (i.e., only the first ten radial modes included in summation), with ten additional modes added in each additional band, reaching up to $S_{\mathrm{max}} = 40$.

APPENDIX I: CONVERGENCE OF THE NUMERICAL COMPUTATIONS

Numerical evaluation of scattered [see Eq. (B9)] and guided [see Eq. (C24)] energies requires summing over azimuthal harmonics $n = 0, \pm 1, \pm 2, \dots$, with the guided energy also requiring summation over the radial harmonics $s = 1, 2, 3, \dots$. In practice, both summations must be truncated at some limit bound N_{max} and S_{max}, such that only indices in the range $n = -N_{\mathrm{max}}, \dots, N_{\mathrm{max}}$ and $s = 1, \dots, S_{\mathrm{max}}$ participate in the summation. In this section, we determine the values of N_{max} and S_{max} required for sufficient convergence for both the scattered and guided energies, following the preliminary assumption that the (normalized) frequency may be truncated from above by $\bar{\omega}_{\mathrm{co}} = 10\pi$.

Figure 13 plots the evaluated scattered and guided energy as a function of truncation bounds, N_{max} for the scattered energy, and both N_{max} and S_{max} for the guided energy, for both low and high energies. The parameters $\varepsilon_r = 12$ and $\eta = 1.05$ were used in simulation, as they essentially represent the extreme case in terms of the number harmonics required for convergence. It can be seen that for both energies the curves "plateau" for $N_{\mathrm{max}} = 30$ in the case of scattered radiation, and $N_{\mathrm{max}} = 40$ for guided radiation, indicating that $N_{\mathrm{max}} = 40$ is sufficient for convergence in terms of the azimuthal harmonics. As for the guided radiation [see Fig. 5(b)], the curves approach a limiting height at about $S_{\mathrm{max}} = 40$, therefore taking the first 40 radial modes yields decent convergence.

---

[1] V. L. Ginzburg and I. M. Frank, Radiation of a uniformly moving electron due to its transition from one medium into another, Zh. Eksp. Teor. Fiz. **9**, 353 (1945).

[2] A. P. Potylitsyn, M. I. Ryazanov, M. N. Strikhanov, and A. A. Tishchenko, *Diffraction Radiation from Relativistic Particles* (Springer, New York, 2011).

[3] J. D. Jackson, *Classical Electrodynamics* (John Wiley & Sons, New York, NY, 1999).

[4] P. A. Cherenkov, Visible light from clear liquids under the action of gamma radiation, Comptes Rendus (Doklady) de l'Aeademie des Sciences de l'URSS **2**, 451 (1934).

[5] S. J. Smith and E. Purcell, Visible light from localized surface charges moving across a grating, Phys. Rev. **92**, 1069 (1953).

[6] R. J. England, R. J. Noble, K. Bane, D. H. Dowell, C.-K. Ng, J. E. Spencer, S. Tantawi, Z. Wu, R. L. Byer, E. Peralta *et al.*, Dielectric laser accelerators, Rev. Mod. Phys. **86**, 1337 (2014).

[7] E. Ruska, The development of the electron microscope and of electron microscopy, Rev. Mod. Phys. **59**, 627 (1987).

[8] S. E. Korbly, A. S. Kesar, J. R. Sirigiri, and R. J. Temkin, Observation of Frequency-Locked Coherent Terahertz Smith-Purcell Radiation, Phys. Rev. Lett. **94**, 054803 (2005).

[9] X. Bendana, A. Polman, and F. J. García de Abajo, Single-photon generation by electron beams, Nano Lett. **11**, 5099 (2011).

[10] M. Lampel, Coherent Smith-Purcell radiation as a pulse length diagnostic, Nucl. Instrum. Methods Phys. Res., Sect. A **385**, 19 (1997).

[11] S. Banna, A. Ludwig, and L. Schächter, Wake-field in an array of metallic posts: Possible application for beam position monitoring, Nucl. Instrum. Methods Phys. Res., Sect. A **555**, 101 (2005).

[12] K. Soong and R. L. Byer, Design of a subnanometer resolution beam position monitor for dielectric laser accelerators, Opt. Lett. **37**, 975 (2012).

[13] R. F. Egerton, *Electron Energy-Loss Spectroscopy in the Electron Microscope* (Springer, New York, 2011).

[14] F. J. Garcia De Abajo, Optical excitations in electron microscopy, Rev. Mod. Phys. **82**, 209 (2010).

[15] H. Lichte and M. Lehmann, Electron holography: Basics and applications, Rep. Prog. Phys. **71**, 016102 (2008).
[16] A. Sommerfeld, Ueber die fortpflanzung elektrodynamischer wellen längs eines drahtes, Ann. Phys. (Leipzig) **303**, 233 (1899).
[17] D. Hondros and P. Debye, Elektromagnetische wellen an dielektrischen drähten, Ann. Phys. (Leipzig) **337**, 465 (1910).
[18] J. R. Wait, Scattering of a plane wave from a circular dielectric cylinder at oblique incidence, Can. J. Phys. **33**, 189 (1955).
[19] J. R. Carson, S. P. Mead, and S. Schelkunoff, Hyper-frequency wave guides: Mathematical theory, Bell Syst. Tech. J. **15**, 310 (1936).
[20] D. Schieber and L. Schächter, Wake field of an electron bunch moving parallel to a dielectric cylinder, Phys. Rev. E **64**, 056503 (2001).
[21] A. A. Saharian, L. S. Grigoryan, A. K. Grigorian, H. F. Khachatryan, and A. S. Kotanjyan, Cherenkov radiation and emission of surface polaritons from charges moving paraxially outside a dielectric cylindrical waveguide, Phys. Rev. A **102**, 063517 (2020).
[22] S. Banna, L. Schächter, and D. Schieber, Wake-field generated by a line charge moving in the vicinity of a dielectric cylinder, Nucl. Instrum. Methods Phys. Res., Sect. A **489**, 18 (2002).
[23] D. O. Yevtushenko, S. V. Dukhopelnykov, A. Nosich *et al.*, Optical diffraction radiation from a dielectric and a metal nanowire excited by a modulated electron beam, Opt. Quantum Electron. **51**, 29 (2019).
[24] T. Ochiai and K. Ohtaka, Relativistic electron energy loss and induced radiation emission in two-dimensional metallic photonic crystals. I. Formalism and surface plasmon polariton, Phys. Rev. B **69**, 125106 (2004).
[25] S. V. Yalunin, B. Schröder, and C. Ropers, Theory of electron energy loss near plasmonic wires, nanorods, and cones, Phys. Rev. B **93**, 115408 (2016).
[26] D. S. Black, Z. Zhao, K. J. Leedle, Y. Miao, R. L. Byer, S. Fan, and O. Solgaard, Operating modes of dual-grating dielectric laser accelerators, Phys. Rev. Accel. Beams **23**, 114001 (2020).
[27] T. Egenolf, U. Niedermayer, and O. Boine-Frankenheim, Tracking with wakefields in dielectric laser acceleration grating structures, Phys. Rev. Accel. Beams **23**, 054402 (2020).
[28] D. S. Black, U. Niedermayer, Y. Miao, Z. Zhao, O. Solgaard, R. L. Byer, and K. J. Leedle, Net Acceleration and Direct Measurement of Attosecond Electron Pulses in a Silicon Dielectric Laser Accelerator, Phys. Rev. Lett. **123**, 264802 (2019).
[29] DLMF, NIST Digital Library of Mathematical Functions, edited by F. W. J. Olver, A. B. Olde Daalhuis, D. W. Lozier, B. I. Schneider, R. F. Boisvert, C. W. Clark, B. R. Miller, B. V. Saunders, H. S. Cohl, and M. A. McClain, version 1.1.6, 30 June 2022, http://dlmf.nist.gov/.
[30] H. Kogelnik, Theory of dielectric waveguides, in *Integrated Optics*, edited by T. Tamir (Springer, New York, 1979), Chap. 2, pp. 13–81.
[31] M. J. Weber, *Handbook of Optical Materials* (CRC, Boca Raton, FL, 2018).
[32] L. Schächter, *Beam-Wave Interaction in Periodic and Quasi-Periodic Structures* (Springer, New York, 2013).
[33] H. C. van de Hulst, *Light Scattering by Small Particles* (Courier, New York, 1981).
[34] C. Yeh and F. I. Shimabukuro, *The Essence of Dielectric Waveguides* (Springer, New York, 2008).
[35] M. Abramowitz, I. A. Stegun, and R. H. Romer, *Handbook of Mathematical Functions with Formulas, Graphs, and Mathematical Tables* (Courier Corporation, North Chelmsford, MA, 1988).
[36] I. S. Gradshteyn and I. M. Ryzhik, *Table of Integrals, Series, and Products* (Academic, New York, 2014).
[37] J. H. Graf, Ueber die addition und subtraction der argumente bei bessel'schen functionen nebst einer anwendung, Math. Ann. **43**, 136 (1893).